

1 **Evidence of a dual African and Australian biomass burning**
2 **influence on the vertical distribution of aerosol and carbon**
3 **monoxide over the Southwest Indian Ocean basin in early 2020**

4 Nelson Bègue¹, Alexandre Baron^{2,3}, Gisèle Krysztofiak⁴, Gwenaël Berthet⁴, Corinna
5 Kloss^{*4a}, Fabrice Jégou⁴, Sergey Khaykin⁶, Marion Ranaivombola¹, Tristan Millet¹,
6 Thierry Portafaix^{1a,b}, Valentin DufLOT^{*1}, Philippe Keckhut⁶, Hélène Vèrèmes¹,
7 Guillaume Payen⁷, Mahesh Kumar Sha⁸, Pierre-François Coheur⁹, Cathy Clerbaux^{9,10},
8 Michaël Sicard¹, Tetsu Sakai¹¹, Richard Querel¹², Ben Liley¹², Dan Smale¹², Isamu
9 Morino¹³, Osamu Uchino^{11,13}, Tomohiro Nagai¹¹, Penny Smale¹², John Robinson¹² and
10 Hassan Bencherif^{1,5}

11 [1] Laboratoire de l'Atmosphère et des Cyclones, UMR 8105 CNRS, Université de la Réunion,
12 Reunion Island, France.

13 [2] Cooperative Institute for Research in Environmental Sciences (CIRES), University of
14 Colorado, Boulder, CO 80305, USA

15 [3] NOAA Chemical Sciences Laboratory (CSL), 325 Broadway, Boulder, CO 80305, USA

16 [4] Laboratoire de Physique et Chimie de l'Environnement et de l'Espace (LPC2E), Université
17 d'Orléans, CNRS UMR7328, Orléans, France.

18 [5] School of Chemistry and Physics, University of KwaZulu-Natal, Durban 4041, South Africa

19 [6] Laboratoire Atmosphères, Observations Spatiales (LATMOS), IPSL, UVSQ Université
20 Paris-Saclay, Sorbonne Université, CNRS, Guyancourt, France

21 [7] Observatoire des Sciences de l'Univers de La Réunion (OSU-Réunion), UAR3365, Saint-
22 Denis de la Réunion, France

23 [8] Royal Belgian Institute for Space Aeronomy (BIRA-IASB), Brussels, Belgium

24 [9] Université libre de Bruxelles (ULB), Spectroscopy, Quantum Chemistry and Atmospheric
25 Remote Sensing (SQUARES), Brussels 1050, Belgium; Bruxelles (ULB), Brussels 1050,
26 Belgium.

27 [10] Laboratoire Atmosphères, Observations Spatiales (LATMOS), IPSL, Sorbonne
28 Université, UVSQ, CNRS, Paris, France

29 [11] Meteorological Research Institute, 1-1 Nagamine, Tsukuba, Ibaraki 305-0052, Japan

30 [12] National Institute of Water & Atmospheric Research (NIWA), Lauder, New Zealand

31 [13] National Institute for Environmental Studies, Tsukuba, Japan

Mis en forme : Justifié

~~*^a now at Forschungszentrum Jülich GmbH~~*now at: Institute for Energy and Climate
Research - Stratosphere (IEK-7), Forschungszentrum Jülich, Jülich, Germany
~~**now at: Department for Atmospheric and Climate Research, NILU – Norwegian Institute for
Air Research, Kjeller, Norway~~

Correspondence to: N.Bègue (nelson.begue@univ-reunion.fr)

Abstract

The pristine atmosphere of the southwest Indian Ocean (SWIO) basin underwent significant perturbations during the 2020 austral summer. This study documents the complex variability of aerosols and carbon monoxide (CO) over this remote oceanic region and identifies the processes governing it in the upper troposphere – lower stratosphere (UT-LS). Aerosol profiles exhibit a multi-layer structure in the tropical UT-LS in January and February 2020. The numerical models (FLEXPART and MIMOSA) showed that the modulation of the aerosol content in the lower stratosphere is due to the intense and persistent stratospheric aerosol layer generated during the 2019–20 extreme Australian bushfire events. One part of this stratospheric aerosol layer was advected zonally by the prevailing easterly winds and its passage over Reunion was recorded by increased aerosol extinction profiles on 27th and 28th January. The analysis of the advected potential vorticity highlights an isentropic transport of air masses containing Australian biomass burning aerosol from extra-tropical latitudes to Reunion at the 400 K isentropic level, on 28th January. Interestingly, our results show that the biomass burning (BB) activity in eastern Africa, weak during this season, contributed to modulating (by up to 90%) the vertical distribution of CO and aerosols in the upper troposphere over the SWIO basin. The simultaneous presence of African and Australian aerosol layers has been recorded by ground-based observations at Reunion. This study highlights for the first time the influence of the African emissions from BB to the CO and aerosol distribution in the upper troposphere over the SWIO basin during the convective season. The results show that besides PyroCb-driven injection of BB products to the stratosphere, an alternative pathway may exist during the regular deep convection season in the tropics. During the 2020 austral summer, the pristine atmosphere of the southwest Indian Ocean (SWIO) basin experienced significant perturbations. This study examines the variability of aerosols and carbon monoxide (CO) over this remote oceanic region and investigates the underlying processes in the upper troposphere – lower stratosphere (UT-LS). Aerosol profiles in January and February 2020 revealed a multi-layer structure in the tropical UT-LS. Numerical models (FLEXPART and MIMOSA) indicated that the lower

Code de champ modifié

Mis en forme : Couleur de police : Automatique

Mis en forme : Police : Non Gras, Couleur de police : Automatique

Mis en forme : Couleur de police : Automatique

Mis en forme : Police : Non Gras, Couleur de police : Automatique

Mis en forme : Couleur de police : Automatique

Mis en forme : Police : Non Gras, Couleur de police : Automatique

Mis en forme : Couleur de police : Automatique

Mis en forme : Police : Non Gras, Couleur de police : Automatique

Mis en forme : Couleur de police : Automatique

Mis en forme : Police : Non Gras, Couleur de police : Automatique

Mis en forme : Couleur de police : Automatique

Mis en forme : Police : Non Gras, Couleur de police : Automatique

Mis en forme : Couleur de police : Automatique

Mis en forme : Couleur de police : Automatique

Mis en forme : Police : Non Gras, Couleur de police : Automatique

Mis en forme : Couleur de police : Automatique

Mis en forme : Police : Non Gras, Couleur de police : Automatique

1 [stratospheric aerosol content was influenced by the intense and persistent stratospheric aerosol](#)
2 [layer generated during the 2019-20 extreme Australian bushfire events. A portion of this layer](#)
3 [was transported eastward by prevailing easterly winds, leading to increased aerosol extinction](#)
4 [profiles over Reunion on January 27th and 28th. Analysis of advected potential vorticity](#)
5 [revealed isentropic transport of air masses containing Australian biomass burning aerosols from](#)
6 [extra-tropical latitudes to Reunion at the 400 K isentropic level on January 28th. Interestingly,](#)
7 [we found that biomass burning \(BB\) activity in eastern Africa, though weak during this season,](#)
8 [significantly influenced \(up to 90%\) the vertical distribution of CO and aerosols in the upper](#)
9 [troposphere over the SWIO basin. Ground-based observations at Reunion confirmed the](#)
10 [simultaneous presence of African and Australian aerosol layers. This study provides the first](#)
11 [evidence of African BB emissions impacting CO and aerosol distribution in the upper](#)
12 [troposphere over the SWIO basin during the convective season.](#)

13 **1. Introduction**

14 [Large amounts of aerosols and active trace gases such as carbon monoxide \(CO\) are injected](#)
15 [throughout the atmosphere during biomass burning \(BB\) events. The Southern American and](#)
16 [Southern African regions are recognized to be significant primary sources of carbonaceous](#)
17 [aerosol and active traces gases in the Southern Hemisphere through the BB season from July to](#)
18 [November \(Benecherif et al., 2020; Garstang et al., 1996; Holanda et al., 2020\). Such BB](#)
19 [activities have the potential to modulate the vertical distribution of trace gases and aerosols](#)
20 [from the troposphere to the stratosphere \(Andreae and Merlet, 2001; Duflot et al., 2010; Héron](#)
21 [et al., 2020\). Under favorable meteorological conditions, pyro-convection events can take place](#)
22 [and have the potential to inject soot and smoke directly into the stratosphere \(Dowdy and Pepler,](#)
23 [2018; Fromm et al., 2010\). Radiative impact of the aerosol and traces gases is determined by](#)
24 [abundance, vertical distribution, and atmospheric residence time \(which, in turn, will affect the](#)
25 [resultant horizontal distribution following advection \(Darbyshire et al., 2018; Morgan et al.,](#)
26 [2019\)\). High concentrations of trace gases and aerosol from these fires can be transported far](#)
27 [from the source regions. This intercontinental transport has the potential to affect the](#)
28 [atmospheric composition of regions typically considered as aerosol-free areas.](#)

29 [The southwest Indian Ocean \(SWIO\) basin is known to be one of the few pristine regions on](#)
30 [Earth where the aerosol concentration is mainly governed by sea salts \(Duflot et al., 2022\). The](#)
31 [SWIO basin is characterized by a wet season \(December to April\) and a dry season \(May to](#)
32 [November\). Previous works showed that the atmospheric composition over the SWIO region](#)
33 [during the dry season is driven by the Southern Hemisphere BB activity \(Clain et al., 2009;](#)
34 [Duflot et al., 2022; Edwards et al., 2006; Kaufman et al., 2003; Swap et al., 2003\). These studies](#)

Mis en forme : Police :Non Gras, Couleur de police :
Automatique

Mis en forme : Police :Non Gras, Couleur de police :
Automatique

Mis en forme : Police :Non Gras, Couleur de police :
Automatique

Mis en forme : Police :Non Gras, Couleur de police :
Automatique

Mis en forme : Couleur de police : Automatique

1 pointed out that BB plumes cross South Africa during the dry season, Edwards et al. (2006)
2 revealed that southern African BB emissions mostly find their way into the SWIO basin and
3 follow the five transportation modes identified by Garstang et al. (1996). Being located in the
4 subtropical southern Indian Ocean at the crossroads of the transport pathway bringing air
5 masses from southern Africa, Reunion Island (21,0°S, 55.5°E) is a favorable location to study
6 the effect of this regional transport on atmospheric composition over the SWIO basin. Based
7 on ozone radiosonde and ground-based lidar observations recorded at Reunion, Clain et al.
8 (2009) highlighted a significant annual increase of tropospheric ozone over Reunion Island
9 during August-November period, in phase with the BB season in southern Africa and
10 Madagascar. High concentrations of ozone precursors from these fires are vented into the free
11 troposphere by convection and are subsequently advected into the SWIO basin by westerly
12 winds. In addition to regional transport, the tropical tropospheric composition over the SWIO
13 basin can be modulated by the long-range transport of BB plumes from South America (Duflot
14 et al., 2010, 2022; Zhou et al., 2018). By combining ground-based observations of Carbon
15 monoxide (CO) from a Fourier Transform Infrared (FTIR) spectrometer installed at Reunion
16 and the FLEXPART model simulations, Duflot et al. (2010) showed that southern African and
17 southern American BB events have the potential to inject large amounts of ozone precursors
18 such as CO and aerosols throughout the troposphere over the SWIO basin. The synergy of CO
19 and aerosol observations are helpful in discussions of the influence of BB events on the
20 evolution of the aerosol burden (Bègue et al., 2021; Bencherif et al., 2020; Jones et al., 2001).
21 Most recently, the analysis of Aerosol Optical Depth (AOD) recorded from sun photometer at
22 Reunion over a period of 12 years has been undertaken by Duflot et al. (2022). Duflot et al.
23 (2022) showed that the BB activity explains 67 % of the variability of the AOD, within which
24 the contributions of the BB activity in Southern Africa and southern America are estimated at
25 22% and 20%, respectively. Although Australia is known for its intense BB events (Fromm et
26 al., 2006; 2010; De Laat et al., 2012), the contribution of the Australian BB activity on the
27 observed AOD variability over Reunion is relatively low (4.7 %).
28 The Australian BB activity takes mainly place in the northern part of the continent between
29 September and January (Russel-Smith et al., 2007). Nevertheless, the most disastrous fires burn
30 in the southeastern region of Australia. Extreme fires occurring over southeastern Australia
31 during the austral summer can lead to the development of pyro-convection events (Dowdy and
32 Pepler, 2018; Fromm et al., 2010). Southeastern Australia has a long history of severe pyro-
33 convection events which have significantly impacted the composition of the stratosphere at
34 regional and global scales. The last and largest event occurred during the 2019-20 fire season

Mis en forme : Police :Non Gras

Mis en forme : Police :Non Gras, Couleur de police :
Automatique

Mis en forme : Police :Non Gras, Couleur de police :
Automatique

1 (referred to as “Black Summer”). Previous works reported that this fire season is unrivaled with
2 a surface burnt estimated at 19 million hectares (Boer et al., 2020; Cai et al., 2022; Levin et al.,
3 2021). Furthermore, this extreme fire season can be considered as unprecedented due to
4 persistent planetary scale perturbations induced in the stratosphere (Kablick et al., 2020;
5 Khaykin et al., 2020; Kloss et al., 2021; Ohneiser et al., 2020, 2022; Santee et al., 2022;
6 Schwartz et al., 2020; Solomon et al., 2023; Yu et al., 2020).

7 Kablick et al. (2020) showed at least 18 pyro-convection outbreaks occurred between 29th
8 December 2019 and 12th January 2020 with the largest event occurring around 1st January 2020.

9 Based on satellite observations and Community Earth System Model-Community Aerosol and
10 Radiation Model for Atmospheres (CESM-CARMA) model results, Yu et al. (2021) showed

11 that Australian wildfires burning from December 2019 to January 2020 injected approximately
12 0.9 Tg of smoke into the stratosphere. The analysis of the numerical simulations suggest that
13 the smoke mass contained 2.5% black carbon which induced a 1 K warming in the stratosphere

14 of the Southern Hemisphere mid-latitude for more than 6 months following its injection. The
15 carbon-rich aerosol clouds were confined during their solar-driven rise by a persistent synoptic-

16 scale anticyclone (Kablick et al., 2020; Khaykin et al., 2020). As a consequence, the highly-
17 concentrated absorbing aerosols were lofted into the middle stratosphere, which prolongs their
18 stratospheric residence time and radiative effect on climate. The combustion products injected

19 into the stratosphere were advected by westerly winds and dispersed across all of the Southern
20 Hemisphere extra-tropical latitudes (Khaykin et al., 2020; Ohneiser et al., 2020, 2022; Tencé et
21 al., 2022; Yu et al., 2020). The stratospheric smoke layer was rapidly advected westward and

22 its optical characteristics were measured by the lidar system installed at Punta Arena (53.2°S,
23 70.9°E; Chile) and Rio Grandé (53.8°S, 67.7°W, Argentina) one week following its injection
24 (Ohneiser et al., 2022). Ohneiser et al. (2022) pointed out that the presence of the smoke layers

25 extended, on average, from 9 to 24 km in height, with one part ascending to more than 30 km
26 height as a result of self-lofting processes. The maximum smoke AOD was around 1.0 over
27 Punta Arenas in January 2020 and thus 2 to 3 orders of magnitude above the stratospheric

28 aerosol background of 0.005 (Ohneiser et al., 2022). Their results suggest an influence of this
29 stratospheric smoke layer on the record-breaking ozone hole over Antarctica in September-
30 November 2020. This is consistent with the results reported by Tencé et al. (2022) from lidar

31 and ozonesonde measurements at the French Antarctic station Dumont d’Urville
32 (66.6°S, 140.0°E). Tencé et al. (2022) pointed out the persistence of aerosol layer in the southern
33 high-latitude stratosphere following the pyro-convection events. They also reported that the

34 2020 stratospheric ozone depletion is above the decadal average at Dumont d’Urville. The

Mis en forme : Police :Non Gras, Couleur de police :
Automatique

Mis en forme : Couleur de police : Automatique

Mis en forme : Police :Non Gras, Couleur de police :
Automatique

Mis en forme : Couleur de police : Automatique

Mis en forme : Police :Non Gras, Couleur de police :
Automatique

Mis en forme : Couleur de police : Automatique

Mis en forme : Police :Non Gras

Mis en forme : Police :Non Gras

Mis en forme : Police :Non Gras, Couleur de police :
Automatique

Mis en forme : Couleur de police : Automatique

1 common point among these studies is their interest for the perturbation induced by the 2019-20
2 Australian fires on the stratospheric composition, and on the dynamical circulation over the
3 extra-tropical latitudes. In contrast, relatively little attention has been paid to the perturbation
4 induced by this Australian BB layer over the tropical/subtropical latitudes.

5 This study has two aims: 1) document the transport of the Australian smoke layer in the southern
6 subtropics over Indian Ocean during the January-February period which correspond to the wet
7 season, and 2) to investigate the influence of Australian aerosol layer on variability of the
8 aerosol optical properties and CO in the Upper Troposphere-Lower Stratosphere (UT-LS) of
9 the SWIO basin accounting for convective activity. Convective activity is more intense during
10 this season as the Inter-Tropical Convergence Zone (ITCZ) is present over the whole basin
11 (Lashkari et al., 2017). Furthermore, the convective activity is often synonym of tropical
12 depression which can reach the stage of tropical cyclone (Barthe et al., 2021; Neuman et al.,
13 1993). The Regional Specialized Meteorological Centre (RSMC) at Reunion reported that the
14 cyclonic season 2019-20 was characterized by the development of 6 tropical cyclones and 4
15 tropical storms in the SWIO basin.

16 The study is organized as follows: Section 2 describes the observations and the model used for
17 the investigation of the transport of the aerosol layer. A review of the formation and the
18 transport of the Australian aerosol layer over the Southern Hemisphere is provided in Section
19 3. An analysis of the influence of the Australian BB plume on the aerosol and CO variability
20 over the SWIO basin is given in Section 4. The discussion on the influence of the convective
21 activity on the transport of the aerosol smoke layer over the SWIO basin is provided in Section
22 5. A summary and the perspectives of this study are given in Section 6.

23 Significant amounts of aerosols and trace gases, such as carbon monoxide (CO), are released
24 into the atmosphere during biomass burning (BB) events in the Southern Hemisphere,
25 particularly in Southern America and Southern Africa from July to November (Bencherif et al.,
26 2020; Garstang et al., 1996; Holanda et al., 2020). These activities disrupt the vertical
27 distribution of gases and aerosols, potentially reaching the stratosphere (Andreae and Merlet,
28 2001; Héron et al., 2020). Under specific meteorological conditions, pyro-convection events
29 can directly inject soot and smoke into the stratosphere (Dowdy and Pepler, 2018; Fromm et
30 al., 2010). The radiative impact of these particles and gases depends on their abundance, vertical
31 distribution, and residence time, influencing their dispersion (Darbyshire et al., 2018; Morgan
32 et al., 2019). Transported over long distances, these aerosols and gases can affect the
33 composition of traditionally aerosol-free regions.

Mis en forme : Police :Non Gras, Couleur de police :
Automatique

Mis en forme : Couleur de police : Automatique

Mis en forme : Police :Non Gras, Couleur de police :
Automatique

Mis en forme : Couleur de police : Automatique

Mis en forme : Police :Non Gras, Couleur de police :
Automatique

Mis en forme : Police :Non Gras, Couleur de police :
Automatique

Mis en forme : Couleur de police : Automatique

Mis en forme : Police :Non Gras, Couleur de police :
Automatique

Mis en forme : Couleur de police : Automatique

1 [The southwest Indian Ocean \(SWIO\) basin stands out as one of the Earth's pristine regions](#)
2 [where aerosol concentration is predominantly governed by sea salts \(Dufлот et al., 2022\).](#)
3 [Characterized by a wet season \(December to April\) and a dry season \(May to November\), the](#)
4 [SWIO region's atmospheric composition during the dry season is significantly influenced by](#)
5 [Southern Hemisphere BB activity \(Clain et al., 2009; Edwards et al., 2006; Kaufman et al.,](#)
6 [2003; Swap et al., 2003\). Studies have highlighted the crossing of BB plumes over South Africa](#)
7 [during the dry season, with southern African BB emissions primarily reaching the SWIO basin](#)
8 [via five identified transportation modes \(Edwards et al., 2006; Garstang et al., 1996\). Situated](#)
9 [in the subtropical southern Indian Ocean at the convergence of air masses from southern Africa,](#)
10 [Reunion Island \(21.0°S, 55.5°E\) provides an ideal location to study the impact of regional](#)
11 [transport on atmospheric composition over the SWIO basin. Ozone radiosonde and ground-](#)
12 [based lidar observations at Reunion have revealed a significant annual increase in tropospheric](#)
13 [ozone during the August-November period, aligned with the BB season in southern Africa and](#)
14 [Madagascar \(Clain et al., 2009\).](#)
15 [Additionally, long-range transport of BB plumes from South America can influence the tropical](#)
16 [tropospheric composition over the SWIO basin \(Dufлот et al., 2010 2022; Zhou et al., 2018\).](#)
17 [By combining ground-based observations of carbon monoxide \(CO\) from a Fourier Transform](#)
18 [Infrared \(FTIR\) spectrometer installed at Reunion with FLEXPART model simulations, Dufлот](#)
19 [et al. \(2010\) demonstrated the potential of southern African and southern American BB events](#)
20 [to inject substantial amounts of ozone precursors such as CO and aerosols throughout the](#)
21 [troposphere over the SWIO basin. This synergy of CO and aerosol observations aids in](#)
22 [understanding the influence of BB events on aerosol burden evolution \(Bègue et al., 2021;](#)
23 [Bencherif et al., 2020; Jones et al., 2001\). Recent analysis of Aerosol Optical Depth \(AOD\)](#)
24 [from sun-photometer data at Reunion over 12 years by Dufлот et al. \(2022\) revealed that BB](#)
25 [activity explains 67% of AOD variability, with Southern Africa and southern America](#)
26 [contributing 22% and 20%, respectively. Despite Australia's reputation for intense BB events](#)
27 [\(Fromm et al., 2006; 2010; De Laat et al., 2012\), its contribution to observed AOD variability](#)
28 [over Reunion is relatively low \(4.7%\).](#)
29 [The Australian BB activity primarily occurs in the northern part of the continent between](#)
30 [September and January, although the most severe fires typically occur in southeastern Australia.](#)
31 [Extreme fires in this region during the austral summer can lead to pyro-convection events, with](#)
32 [a significant impact on the stratosphere at regional and global scales. The unprecedented 2019-](#)
33 [20 fire season, known as the "Black Summer," witnessed numerous pyro-convection outbreaks,](#)
34 [injecting approximately 0.9 Tg of smoke into the stratosphere \(Yu et al., 2021\). This smoke](#)

1 [mass, containing 2.5% black carbon, induced a 1 K warming in the stratosphere of the Southern](#)
2 [Hemisphere mid-latitude for more than 6 months following its injection. The smoke layer was](#)
3 [advected by westerly winds, dispersing across all extra-tropical latitudes in the Southern](#)
4 [Hemisphere. The optical characteristics of the stratospheric smoke layer were measured by lidar](#)
5 [systems in Chile and Argentina, with the smoke layer extending from 9 to over 30 km in height](#)
6 [\(Ohneiser et al., 2022\). The presence of this smoke layer significantly impacted the record-](#)
7 [breaking ozone hole over Antarctica in September-November 2020, as reported by Tencé et al.](#)
8 [\(2022\). Despite the extensive research on the impact of Australian fires on the stratospheric](#)
9 [composition and circulation over extra-tropical latitudes, relatively little attention has been paid](#)
10 [to their influence over tropical/subtropical latitudes.](#)

11 [This study aims to document the transport of the Australian smoke layer in the southern](#)
12 [subtropics over the Indian Ocean during the January-February period, corresponding to the wet](#)
13 [season in the SWIO basin. The intensity of convective activity during this season, with the](#)
14 [presence of the Inter-Tropical Convergence Zone \(ITCZ\) over the entire basin, often leads to](#)
15 [tropical depressions reaching the stage of tropical cyclones \(Lashkari et al., 2017; Barthe et al.,](#)
16 [2021; Neuman et al., 1993\). The Regional Specialized Meteorological Centre \(RSMC\) at](#)
17 [Reunion reported the development of 6 tropical cyclones and 4 tropical storms in the SWIO](#)
18 [basin during the cyclonic season 2019-20.](#)

19 [The study is structured as follows: Section 2 outlines the observations and the model employed](#)
20 [to investigate aerosol layer transport. Section 3 reviews the formation and transport of the](#)
21 [Australian aerosol layer across the Southern Hemisphere. Section 4 analyzes the impact of the](#)
22 [Australian BB plume on aerosol and CO variability over the SWIO basin. Section 5 discusses](#)
23 [the influence of convective activity on aerosol smoke layer transport over the SWIO basin.](#)
24 [Finally, Section 6 provides a summary and future perspectives of the study.](#)

25 **2. Instrumentation and Model description**

26 **2.1 Aerosols data sets**

27 The aerosol datasets used in this study resulted mainly from two ground-based observations
28 sites from the Network for the Detection of Atmospheric Composition Change (NDACC,
29 www.ndacc.org) network as well as a suite of spaceborne sensors products.

30 **2.1.1 Lauder ground-based lidar**

31 Measurements of aerosol optical properties at Lauder (45.0°S; 169.7°E) have been performed
32 using lidars since 1992. [The lidar system, detailed by Sakai et al. \(2016\), utilizes a Nd:YAG](#)
33 [laser beam at 532 nm with linear polarization. A detailed description of the lidar system](#)

Code de champ modifié

operating at Lauder is given by Sakai et al. (2016), and it is summarized hereafter. The emitter system consists of a Nd:YAG laser beam at 532 nm and is linearly polarized. The lidar detects Rayleigh-Mie backscattering at 532 nm with parallel and perpendicular components. Extinction and backscatter coefficients were derived using the methodology outlined by Fernald et al. (1984), incorporating an aerosol extinction-to-backscatter ratio, known as the lidar ratio (LR). LR values for January-May 2020 are 88 sr and 60 sr for altitudes above and below 23 km, respectively, determined through signal attenuation methodology described by Uchino et al. (1983) and Young (1995). This methodology involves the use of an extinction to backscatter ratio for aerosol, also called lidar ratio (LR). For the January-May 2020 period, the values of LR derived with the lidar, are 88 and 60 sr for altitude above and below 23 km respectively. These values are obtained from the attenuation of the lidar signals by using the methodology described by Uchino et al. (1983) and by Young (1995). The aerosol depolarization is computed from the backscatter coefficient and the total linear volume depolarization ratio (Sakai et al., 2003). This latter is obtained by taking the ratio of the perpendicular to total components of the backscattered signal at 532 nm. Aerosol depolarization was computed from the backscatter ratio and the total linear volume depolarization ratio (Sakai et al., 2003), calculated as the ratio of perpendicular to parallel components of the backscattered signal at 532 nm. To investigate the aerosol variability induced by the Australian fires, it is necessary to define a background profile. The profile is built from measurements performed when atmosphere is not undergoing major disturbance (e.g. volcanic eruptions, pyro convection outbreaks). In the present work, the background extinction profile at Lauder is built from measurements performed between 1997 and 2004. To analyze aerosol variability attributed to Australian fires, a background profile was defined using measurements taken during periods without significant atmospheric disturbances, such as volcanic eruptions or pyro-convection outbreaks. In this study, the background extinction profile at Lauder was constructed from measurements made between 1997 and 2004.

2.1.2 Reunion Island ground-based lidars

The Atmospheric Physics Observatory of La Réunion (OPAR) serves as a permanent station for long term atmospheric observations (Baray et al., 2013). In particular, two lidar systems operating the Maïdo Observatory, situated at 2200 m above mean sea level (AMSL), in the UV (355 nm) and visible part of the light spectrum (532 nm) are used to retrieve ozone and aerosols profiles at the Maïdo Observatory situated at 2200 m above mean sea level (AMSL). retrieve ozone and aerosol profiles in the UV (355 nm) and visible (532 nm) parts of the light spectrum. These systems, LiO3T (532 nm) and LiO3S (355 nm), are described by Baray et al. (2006).

Mis en forme : Couleur de police : Automatique

Mis en forme : Police : Non Gras, Couleur de police : Automatique

Mis en forme : Couleur de police : Automatique

Mis en forme : Police : Non Gras, Couleur de police : Automatique

Mis en forme : Couleur de police : Automatique

1 Extending from approximately 15 km to the middle stratosphere (~35 km), these lidars provide
2 high-resolution aerosol optical property measurements (extinction, backscatter ratio) with a
3 vertical resolution of 15 m. By employing two distinct wavelengths, the Reunion lidar profiles
4 facilitate the assessment of the Angström exponent of aerosols between 355 nm and 532 nm,
5 providing insight into the aerosol's extinction behavior and microphysical properties,
6 particularly particle size. A small Angström exponent typically indicates a coarse mode driving
7 the aerosol's optical properties. Further details on the Angström exponent, aerosol size, and
8 their relative error concerning extinction properties are elaborated in Baron et al. (2023) and its
9 supplementary information. The inversion process in this study utilized the Klett method (Klett,
10 1985), assuming a lidar ratio of 60 sr, typical of aged biomass burning (BB) aerosols (Müller
11 et al., 2007). Nine lidar profiles recorded during the January-March 2020 period were
12 employed, with the background extinction profile at Reunion constructed from measurements
13 taken between 2017 and 2019, excluding the perturbation induced by the Calbuco eruption in
14 April 2015 (Bègue et al., 2017). These systems, named LiO3T (532 nm) and LiO3S (355 nm)
15 are described by Baray et al. (2006), respectively. These lidars measure aerosol optical
16 properties (extinction, backscatter ratio) from ~15 km to the middle stratosphere, up to ~35 km,
17 with a high vertical resolution (15 m). Operating at two distinct wavelengths, the synergy of
18 Reunion lidar profiles allows us to assess the Angström exponent of aerosols between 355 nm
19 and 532 nm. The Angström exponent is a parameter informing on the extinction behavior of the
20 atmospheric constituent with the light spectrum. It is often used to infer some microphysical
21 properties of aerosol and in particular some information on the particle size. In general, a small
22 Angström exponent is synonym of a coarse mode driving the optical properties of the aerosol.
23 Insight on the Angström exponent and aerosol size as well as its relative error with respect to
24 extinction properties are developed in Baron, et al, 2023 and its attached supplementary
25 information. In this study, the inversion process used the Klett method (Klett, 1985) with an
26 assumed lidar ratio of 60 sr, typical of aged BB aerosols (Müller et al., 2007). In the present
27 study we used 9 lidar profiles recorded during the January-March 2020 period. The background
28 extinction profile at Reunion is built from measurements performed between 2017 and 2019
29 excluding the perturbation induced by the Calbuco eruption in April 2015 (Bègue et al., 2017).
30 Although the lidar systems used in this study are different builds, extinction profiles at 532 nm
31 from Lauder and Reunion can be compared to infer the evolution of the plume optical
32 properties.

2.1.3 CALIOP

Mis en forme : Police :Non Gras, Couleur de police :
Automatique

Mis en forme : Couleur de police : Automatique

Mis en forme : Police :Non Gras, Couleur de police :
Automatique

1 Cloud-Aerosol Lidar with Orthogonal Polarization (CALIOP) is a nadir pointing lidar orbiting
2 the Earth onboard the Cloud-Aerosol Lidar and Infrared Pathfinder Satellite Observation
3 (CALIPSO) satellite since 2006. [CALIOP operates at two wavelengths \(532 and 1064 nm\) and](#)
4 [measures total attenuated backscatter vertical profiles with altitude-varying vertical \(30–300 m\)](#)
5 [and horizontal \(300–5000 m\) resolution. CALIOP is a two-wavelength-polarization-sensitive](#)
6 [lidar \(532 and 1064 nm\) that measures total attenuated backscatter vertical profiles with](#)
7 [altitude-varying vertical \(30–300 m\) and horizontal \(300–5000 m\) resolution.](#) In the present
8 study, we used CALIOP product version 3.3 level 1B which includes calibrated attenuated
9 backscatter along with collocated meteorological information provided by the National
10 Aeronautics and Space Administration Global Modeling and Assimilation Office (GMAO).
11 These data [undergo postprocessing](#) ~~are postprocessed~~ using a treatment described and validated
12 by Vernier et al. (2009). ~~The~~ Scattering Ratio (SR) profiles used for the detection of the smoke
13 plume are calculated following the methodology described by Khaykin et al. (2018).
14 ~~Initially, As a first step,~~ the collocated GMAO data ~~is used to~~ correct the backscatter profiles of
15 molecular attenuation and ozone absorption. ~~Subsequently Then,~~ the SR ~~was~~ calculated as the
16 ratio of total and molecular backscatter coefficients, with the latter derived from GMAO air
17 density. ~~The~~ SR profiles ~~were~~ ~~are~~ recalibrated at 36–39 km, following the methodology given
18 by Vernier et al. (2009). ~~The~~ ~~d~~ Data with depolarization larger than 30 % ~~were~~ ~~are~~ discarded to
19 the treatment in order to avoid aliasing cirrus clouds above the thermal tropopause. ~~The~~
20 CALIOP data were obtained from the ACDISC data archive (<ftp://acdisc.gsfc.nasa.gov>) hosted
21 by NASA Goddard Space Flight Center.

22 **2.1.4 Sun photometry measurements: Sky radiometer**

23 ~~A sky radiometer is a scanning sun-sky photometer able to perform measurements of direct sun~~
24 ~~and diffuse sky irradiance under clear sky conditions, at seven wavelengths (between 315 and~~
25 ~~1020 nm) and at several scattering angles. The direct solar extinction and diffuse sky radiance~~
26 ~~measurements are used to derive the aerosol optical properties such as Aerosol Optical Depth~~
27 ~~(AOD), Single Scattering Albedo (SSA) and aerosol size distributions using the algorithm~~
28 ~~developed by Nakajima et al. (1996). A detailed description of the sky radiometer and the~~
29 ~~associated data retrieval is given by Hashimoto et al. (2012). In the present study, we used the~~
30 ~~sky radiometer observations performed at Lauder in the framework of the SKYNET network.~~
31 ~~SKYNET is a ground-based network of sky radiometers with observation sites spread over Asia~~
32 ~~and other areas. Previous works have shown that the AOD from SKYNET is obtained with high~~
33 ~~accuracy similar with that of the standard Langley method and with those from AERONET~~
34 ~~(Campanelli et al., 2007; Che et al., 2008). At Lauder, the sky radiometer measurements have~~

1 ~~been made since 2011. These observations are used in the present study to investigate the~~
2 ~~aerosol variability induced by the passage of the Australian BB plume over Lauder. The~~
3 ~~background evolution of AOD is built with measurements performed between 2011 and 2018.~~
4 ~~The sky radiometer data used in this work are available on : <https://www.skynet-isdc.org/>~~

Code de champ modifié

5 **2.1.45 OMPS-LP**

6 The Ozone Mapper and Profiler Suite Limb profiler (OMPS-LP) has been ~~operational flying~~
7 ~~on the Suomi National Polar Partnership (NPP) satellite platform since October 2011. In this~~
8 ~~present study, we utilized~~ aerosol extinction profiles from the NASA OMPS data product
9 version 2.0 (Taha et al., 2021). ~~These aerosol extinction profiles were are~~ retrieved from the
10 limb scattering solar radiation ~~measurements at wavelengths of 510, 600, 675, 745, 869, and~~
11 ~~997 nm, chosen to minimize the impact of gaseous absorption. The V2.0 algorithm uses OMPS-~~
12 ~~LP measurements at wavelengths 510, 600, 675, 745, 869 and 997 nm, selected to minimize~~
13 ~~the effect of gaseous absorption (Taha et al., 2021).~~ Aerosol extinction measurements are
14 provided from 10 to 40 km altitude on a 1 km vertical grid, ~~resulting in near-global coverage~~
15 ~~every 3-4 days. A near global coverage is produced within 3-4 days.~~ The OMPS data ~~were are~~
16 ~~employed used in the present study~~ to investigate the global transport of aerosol BB plumes and
17 ~~their its~~ influence on the aerosol variability over Reunion. ~~Following the recommendation of~~
18 ~~As recommended by~~ Taha et al. (2021), we used aerosol extinction measurements at 745 nm.
19 ~~The background extinction profile was constructed using measurements obtained from 2012 to~~
20 ~~2014 and from 2016 to 2018, excluding periods affected by the Calbuco eruption (Bègue et al.,~~
21 ~~2015). The background extinction profile is built with measurements performed from 2012 to~~
22 ~~2014 and from 2016 to 2018. These periods are chosen in order to discard the perturbation~~
23 ~~induced by the Calbuco eruption (Bègue et al., 2015).~~ The OMPS data are downloaded from:
24 ~~<https://ozoneaq.gsfc.nasa.gov/>.~~

Code de champ modifié

25 ~~Additionally, The we utilized~~ aerosol absorbing index (AAI) data from OMPS ~~to characterize~~
26 ~~are also used to describe~~ the transport of the aerosol BB plume. ~~The AAI enables the detection~~
27 ~~of absorbing aerosols by quantifying the spectral difference between specific pairs of UV~~
28 ~~wavelengths. Positive AAI values indicate the presence of UV-absorbing aerosols such as dust~~
29 ~~and smoke, while negative values suggest non-absorbing aerosols. Values close to zero~~
30 ~~typically correspond to the presence of clouds. This index allows the detection of absorbing~~
31 ~~aerosols through the spectral difference between a given pair of UV wavelength. When its value~~
32 ~~is positive, it indicates the presence of UV absorbing aerosols such as dust and smoke.~~
33 ~~Conversely, a negative value indicates the presence of non absorbing aerosols while values~~

1 ~~close to zero are found in the presence of clouds.~~ The AAI data used in this work are available
2 on the NASA Earth Data platform: <https://earthdata.nasa.gov/earth-observation-data>

Code de champ modifié

3 **2.2 CO and water vapor measurements**

4 **2.2.1 FTIR**

5 ~~The total columns and volume mixing ratio profiles of trace gases such as CO are retrieved with~~
6 ~~high accuracy and precision with ground-based Fourier Transform Infrared (FTIR)~~
7 ~~spectrometers (Clerbaux et al., 2008; Vigouroux et al., 2015; Zhou et al., 2019). Ground-based~~
8 ~~Fourier Transform Infrared (FTIR) spectrometers enable the retrieval of total columns and~~
9 ~~volume mixing ratio profiles of trace gases like CO with high accuracy and precision (Clerbaux~~
10 ~~et al., 2008; Vigouroux et al., 2015; Zhou et al., 2019). In the present study, we use the FTIR~~
11 ~~observations from performed at Lauder and Reunion- conducted as part of sites the framework~~
12 ~~of the NDACC and Total Carbon Column Observing Network (TCCON) networks~~
13 ~~respectively, are utilized. The FTIR systems and data retrieval methods are extensively~~
14 ~~described by de Mazière et al. (2018) and Wunch et al. (2015). A detailed description of the~~
15 ~~FTIR systems involved in both networks and the associated data retrieval is given by de Mazière~~
16 ~~et al. (2018) and Wunch et al. (2015). A brief description is given hereafter. The CO~~
17 ~~measurements from FTIR a~~

18 ~~At Lauder, CO measurements~~ have been made since the early 1990s. ~~The measurements are~~
19 ~~made~~ using a Bruker high-resolution spectrometer over a wide spectral range (around 600–4500
20 cm^{-1}). The CO dataset used in this study ~~aligns is the same as with~~ that used by Bègue et al.,
21 (2021) and Kloss et al., (2019), ~~providing details on spectral measurements, CO retrieval~~
22 ~~strategy, and derived CO column abundances.~~ ~~Details on the spectral measurements, CO~~
23 ~~retrieval strategy and derived CO column abundances can be found within these references. The~~
24 CO total columns and volume mixing ratio profiles ~~for the Lauder site, spanning a~~ 48-layer
25 atmosphere (0.37–100 km asl), ~~were obtained used in this study for the Lauder site were~~
26 ~~downloaded~~ from the NDACC website (<http://www.ndacc.org>).

Mis en forme : Police :Non Gras, Couleur de police :
Automatique

Code de champ modifié

27 ~~The FTIR measurements a~~ At Reunion, ~~FTIR measurements~~ have been routinely ~~conducted~~
28 ~~since 2011 within the TCCON network using a Bruker high-resolution spectrometer. performed~~
29 ~~in the framework of the TCCON network since 2011. A Bruker high resolution spectrometer~~
30 ~~over a wide spectral range is also used at Reunion. The CO and O₂ total columns are~~
31 ~~simultaneously retrieved by using the GGG2014 code (Wunch et al., 2015). The GGG2014~~
32 ~~code (Wunch et al., 2015) was employed to simultaneously retrieve CO and O₂ total columns.~~
33 ~~The column-averaged dry-air mole fraction of CO was then determined as the ratio between the~~
34 ~~retrieved CO total columns and the total columns of dry air, leveraging the O₂ total columns~~

1 provided by TCCON. CO abundance data for Reunion were sourced from the TCCON database
2 (<https://tccodata.org>). For this study, the background evolution of CO is established using
3 measurements obtained between 2015 and 2018 (De Mazière et al., 2017). Column averaged
4 dry air mole fraction of CO obtained from the retrieval of these two components. TCCON uses
5 the O₂ total to determine the total column of the dry air. Then, the column averaged dry air
6 mole fraction of CO is calculated as the ratio between the retrieved CO total columns and the
7 total columns of the dry air. The abundance of CO used in the study for Reunion are downloaded
8 from the TCCON database (<https://tccodata.org>). In the present study, the background
9 evolution of CO is built with measurements performed between 2015 and 2018 (De Mazière et
10 al., 2017).

11 2.2.2 IASI

12 The Infrared Atmospheric Sounding Interferometer (IASI) utilizes a Fourier Transform spectrometer
13 such as CO by using a Fourier Transform spectrometer to measure chemical species like CO
14 (Clerbaux et al., 2009; Coheur et al., 2009). Operating It is flying on board the three Metop
15 satellites, Retrieval of IASI retrieves CO total and partial columns occurs in near real-
16 time from the nadir radiances measured by the instrument in the thermal infrared covering
17 wavelengths from 6.62 to 15.5 μm. This enables the generation of global distributions for both
18 day and night measurements, covering the troposphere and lower stratosphere. The Fast-
19 Optimal Retrievals on Layers for IASI (FORLI-CO, Hurtmans et al., 2012) was employed to
20 retrieve total and partial CO columns, while also flagging data contaminated by clouds. For this
21 study, CO columns from IASI instruments on Metop-A (operating since 2006) and Metop-B
22 (operating since 2012) are utilized Global distributions are obtained for day and night
23 measurements, with a vertical range covering the troposphere and the lower stratosphere. The
24 total and partial column of CO are retrieved by using the Fast Optimal Retrievals on Layers for
25 IASI (FORLI CO, Hurtmans et al., 2012). Furthermore, the contamination of the data by clouds
26 is checked and flagged. In the present study, we used CO columns from IASI instruments on
27 Metop A and Metop B, which have been operating since 2006 and 2012, respectively. The IASI
28 products used in this study can be accessed work are available on through the AERIS platform:
29 <https://iasi.aeris-data.fr/CO>.

30 2.2.3 MLS

31 The Microwave Limb Sounder (MLS) performs vertical profile measurements of multiple trace
32 gases in the UT-LS onboard Aura satellite since 2004 (Waters et al., 2006). The Microwave
33 Limb Sounder (MLS) on board the Aura satellite has been conducting vertical profile
34 measurements of various trace gases in the UT-LS since 2004 (Waters et al., 2006). In the For

Code de champ modifié

Code de champ modifié

1 ~~this study-present study~~, the CO and water vapor observations (version 5) from January 2017
2 to January 2020 ~~were utilized, covering over~~ a global domain ~~spanningextending~~ between 10°S
3 and 25°S in latitude and 30°E and 60°E in longitude ~~have been used~~. ~~All MLS version 5 retrieval~~
4 ~~quality flags (quality, status, convergence, and precision) were meticulously followed for all~~
5 ~~analyses (Livesey et al., 2022). All MLS version 5 retrieval quality flags (quality, status,~~
6 ~~convergence, and precision) were properly adhered to for all of our analyses (Livesey et al.,~~
7 ~~2020).~~ Generally, ~~The~~ recommended pressure levels for science applications with CO and water
8 vapor MLS data range from 0.0215 to 215 hPa (~~Version 5.0x Level 2 and 3 data quality and~~
9 ~~description document. (nasa.gov)~~). The CO and water vapor profiles from MLS ~~were are~~ obtained
10 from the Atmospheric Composition Data and Information Services Center (ACDISC) archive
11 (~~ftp://acdisc.gsfc.nasa.gov~~) hosted by the NASA Goddard Space Flight Center.

Code de champ modifié

Code de champ modifié

2.3 Numerical Modelling

2.3.1 FLEXPART Model

14 ~~The Lagrangian transport and diffusion model FLEXPART version 10.4 is used to simulate~~
15 ~~long range transport of atmospheric tracers (Pisso et al., 2019; Stohl et al., 2005).~~The
16 ~~Lagrangian transport and diffusion model FLEXPART version 10.4 is utilized in this study to~~
17 ~~simulate the long-range transport of atmospheric tracers (Pisso et al., 2019; Stohl et al., 2005).~~
18 ~~This version of FLEXPART incorporates improvements in various aspects, including~~
19 ~~microphysical and chemical parameterizations (Pisso et al., 2019).~~Source identification was
20 ~~achieved by releasing particles from a receptor location and simulating backward trajectories~~
21 ~~(Seibert and Franck, 2004). Model calculations rely on ERA5 reanalysis meteorological~~
22 ~~observations from ECMWF, extracted at 3-hourly intervals with a horizontal resolution of 0.5°~~
23 ~~× 0.5° and a vertical resolution of 137 hybrid model levels (Hersbach et al., 2020).~~

Mis en forme : Couleur de police : Texte 1

24 ~~This version of FLEXPART includes improvements in different aspects such as microphysical~~
25 ~~and chemical parameterizations (Pisso et al., 2019). Source identification occurs via the release~~
26 ~~of particles from a receptor location and the simulation of backward trajectories. Model~~
27 ~~calculations are based on ERA5 (Hersbach et al., 2020) meteorological data from the European~~
28 ~~Center for Medium Range Weather Forecasts (ECMWF) extracted at 3 hourly intervals with a~~
29 ~~horizontal resolution of 0.5° × 0.5° and a vertical resolution of 137 hybrid model levels (from~~
30 ~~the ground to 0.01 hPa pressure altitude).~~

Mis en forme : Couleur de police : Texte 1

Mis en forme : Police : Non Gras, Couleur de police : Texte 1

Mis en forme : Couleur de police : Texte 1

31 The model simulations ~~involved, are run with the~~ aerosol (Black Carbon-BC and Organic
32 Carbon-OC) and CO tracers, ~~considering assuming~~ removal ~~mechanisms such as by~~ dry and
33 wet deposition for aerosols and OH reactions for CO. ~~The parametrization (default values for~~
34 ~~the scavenging coefficient and the nucleation efficiency and size) for the BC was found in the~~

Mis en forme : Couleur de police : Texte 1

Mis en forme : Police : Non Gras, Couleur de police : Texte 1

Mis en forme : Couleur de police : Texte 1

Mis en forme : Couleur de police : Texte 1

Mis en forme : Couleur de police : Texte 1

1 paper of Grythe et al. (2017) and the chemical parameterization for CO was in default in
2 FLEXPART data but can be found in the reference kinetics database IUPAC (Atkinson et al.,
3 2006). ~~by using parameter from Pisso et al. (2019).~~ Each simulation consists of 20,000 particles
4 released over Reunion ~~daily, during one day~~ at altitudes between 15 and 19 km every 0.5 km,
5 ~~and traces them backward in time over one month, and followed backward in time during one~~
6 ~~month.~~ Simulations of backward trajectories over long periods (1-2 months) have been explored
7 in previous studies (Aliaga et al., 2021; Eckhardt et al., 2017; Xu et al., 2021). The simulations
8 included turbulence parameterization and convection activation (Forster et al.; 2007). ~~The~~
9 ~~simulation of backward trajectories with FLEXPART for a long period (1-2 months) were~~
10 ~~previously explored in previous studies (Aliaga et al., 2021; Eckhardt et al., 2017; Xu et al.,~~
11 ~~2021). The simulations include the parameterization of turbulence and the activation of the~~
12 ~~convection.~~
13 FLEXPART model outputs ~~were are~~ distributed over a regular vertical grid of $0.5^\circ \times 0.5^\circ$
14 from ground level to 25 km in altitude. ~~These, model outputs were are~~ used to assess ~~discuss~~
15 the residence time of the BB aerosols and CO, ~~as well as their contributions to the variability~~
16 ~~of aerosol optical properties and CO over the SWIO basin, and their contributions on the~~
17 ~~variability of the aerosol optical properties and CO over the SWIO basin. Discussions were~~
18 ~~based on emission sensitivity analysis from backward simulations. The residence time of~~
19 ~~particles was integrated over the entire atmospheric column and latitude to create averaged~~
20 ~~maps and longitudinal cross-sections, providing insights into the geographical and vertical~~
21 ~~dispersion of BB aerosols. Discussions are based to the analysis of the emission sensitivity~~
22 ~~obtained from backward simulations. The residence time of particles are integrated over the~~
23 ~~entire atmospheric column and over the latitude to create averaged map and longitudinal cross-~~
24 ~~section map and to provide information on the geographical and vertical dispersion of BB~~
25 ~~aerosols in the atmosphere.~~
26 The BB contributions ~~to on~~ the vertical distribution of CO and the aerosol optical properties
27 ~~were can be~~ calculated by combining the potential emission sensitivity (PES) with an emission
28 inventory, ~~as explained in Stohl et al. (2003), PES represents FLEXPART particles injected at~~
29 ~~the layer/altitude of emissions. Pyro-convection was not considered in the model. BB aerosol~~
30 ~~and CO mass concentration profiles were obtained by summing all output grid points. For BB~~
31 ~~emissions, a layer between 0 and 3 km was used for Africa and between 9 and 16 km for~~
32 ~~Australian fires. PES represents FLEXPART particles only in the layer/altitude at which the~~
33 ~~emissions are injected. Pyro-convection is not taken into account in the model (nor ECMWF~~
34 ~~data). A mass concentration profile of BB aerosol and CO is extracted by summing all the~~

Mis en forme : Couleur de police : Texte 1

Mis en forme : Police :Non Gras, Couleur de police : Texte 1

Mis en forme : Couleur de police : Texte 1

Mis en forme : Couleur de police : Texte 1

Mis en forme : Couleur de police : Texte 1

Mis en forme : Couleur de police : Texte 1

Mis en forme : Couleur de police : Texte 1

Mis en forme : Couleur de police : Texte 1

Mis en forme : Couleur de police : Texte 1

Mis en forme : Couleur de police : Texte 1

Mis en forme : Couleur de police : Texte 1

Mis en forme : Couleur de police : Texte 1

Mis en forme : Couleur de police : Texte 1

Mis en forme : Couleur de police : Texte 1

Mis en forme : Couleur de police : Texte 1

Mis en forme : Police :Non Gras, Couleur de police : Texte 1

Mis en forme : Couleur de police : Texte 1

Mis en forme : Couleur de police : Texte 1

Mis en forme : Couleur de police : Texte 1

Mis en forme : Couleur de police : Texte 1

Mis en forme : Couleur de police : Texte 1

Mis en forme : Couleur de police : Texte 1

Mis en forme : Police :Non Gras, Couleur de police : Texte 1

Mis en forme : Couleur de police : Texte 1

Mis en forme : Police :Non Gras, Couleur de police : Texte 1

Mis en forme : Couleur de police : Texte 1

1 output grid points. A layer between 0 and 3 km is used for the BB in Africa (as observed in
2 [Global Fire Assimilation System](#), "top altitude of plume", Kaiser et al., 2012) and between 9
3 and 16 km for the Australian fires (as observed by CALIOP observations).

4 [The Global Fire Assimilation System \(GFAS\) version 1.2 emission \(Kaiser et al., 2012\) and the](#)
5 [Global Air Pollutant Emissions - EDGAR v6.1 emission inventory](#)
6 [\(http://edgar.jrc.ec.europa.eu\) for CO were utilized. These emissions represent total CO](http://edgar.jrc.ec.europa.eu)
7 [emissions from anthropogenic activities, excluding large scale BB. Multiplying the CO](#)
8 [emission flux from this inventory by the FLEXPART emission sensitivity for a layer between](#)
9 [0 and 1 km provides the contribution of anthropogenic sources to total CO abundance. Finally,](#)
10 [aerosol mass concentration profiles are converted into extinction profiles using the Mie](#)
11 [scattering model, considering spherical particles with a density of 2 g.cm⁻³ and a refractive](#)
12 [index of 2.0 + 0.64i for optically absorbing aerosols.](#)

13 ~~▲~~
14 ~~In the present study, the [Global Fire Assimilation System \(GFAS\) version 1.2 emission \(Kaiser](#)
15 ~~et al., 2012) has been used for the calculation. In addition, the [Global Air Pollutant Emissions](#)
16 ~~–[EDGAR v6.1 emission inventory \(Kaiser et al., 2012, http://edgar.jrc.ec.europa.eu\)](#) is used for~~
17 ~~CO for the year 2018 with a 0.1° × 0.1° grid. These emissions represent the total CO emissions~~
18 ~~by anthropogenic activities excluding large scale BB with Savannah burning, forest fires. As~~
19 ~~for the BB emissions, multiplying the CO emission flux from this inventory with the~~
20 ~~FLEXPART emission sensitivity for a layer between 0 and 1 km gives access to the contribution~~
21 ~~of anthropogenic sources to the total CO abundance. At the end of the process, in the case of~~
22 ~~aerosols, the mass concentration profile is converted in extinction profile in order to evaluate~~
23 ~~the contribution of BB aerosols on the vertical distribution of the aerosol extinction observed~~
24 ~~from Lidar over Reunion. The conversion is performed by the use of Mie scattering model~~
25 ~~assuming spherical particles with a density of 2 g.cm⁻³ and a refractive index of 2.0 + 0.64i~~
26 ~~adapted to optically absorbing aerosols.~~~~~~

27 2.3.2 MIMOSA Model

28 The Modèle Isentropique de transport Mésoéchelle de l'Ozone Stratosphérique par Advection
29 (MIMOSA) model is a potential vorticity (PV) advection model [designed to run running](#) on
30 isentropic surfaces [with a resolution of at a resolution of](#) 0.3° × 0.3° (Hauchecorne et al., 2002).
31 ~~Its~~ The advection scheme is semi-Lagrangian with a time step of 1 h and ~~is~~ driven by ERA5
32 reanalysis meteorological observations. [The model can be continuously run to track the](#)
33 [evolution of PV filaments over several months. The accuracy of the MIMOSA model has been](#)
34 [evaluated and validated in previous studies. Hauchecorne et al. \(2002\) assessed its accuracy.](#)

Mis en forme : Police :Non Gras, Couleur de police : Texte 1

Mis en forme : Couleur de police : Texte 1

Mis en forme : Couleur de police : Texte 1, Anglais (Royaume-Uni)

Mis en forme : Couleur de police : Texte 1

Mis en forme : Police :Non Gras, Couleur de police : Texte 1

Mis en forme : Couleur de police : Texte 1

Mis en forme : Couleur de police : Texte 1

Mis en forme : Couleur de police : Texte 1

Mis en forme : Police :Non Gras, Couleur de police : Texte 1

Mis en forme : Couleur de police : Texte 1

Mis en forme : Anglais (États-Unis)

Mis en forme : Couleur de police : Texte 1

Mis en forme : Couleur de police : Texte 1

Mis en forme : Couleur de police : Texte 1

Mis en forme : Couleur de police : Texte 1

Mis en forme : Police :Non Gras, Couleur de police : Texte 1

Mis en forme : Couleur de police : Texte 1

1 [and it was validated against airborne lidar ozone measurements using a correlation between PV](#)
2 [and ozone, as ozone behaves as a quasi-conserved chemical tracer on timescales of a week or](#)
3 [so within most of the lower stratosphere \(Heese et al., 2001\). Moreover, the MIMOSA model](#)
4 [can be used to determine the origin of air masses influencing a given site, similar to an isentropic](#)
5 [Lagrangian trajectory model. This capability has been demonstrated in various studies](#)
6 [\(Bencherif et al., 2011; Hauchecorne et al., 2002; Portafaix et al., 2003; Bègue et al., 2017\).](#)
7 [The model can be run continuously in order to follow the evolution of PV filaments for several](#)
8 [months. The accuracy of the model has been evaluated by Hauchecorne et al. \(2002\) and](#)
9 [validated against airborne lidar ozone measurements using a correlation between PV and ozone,](#)
10 [a quasi conserved chemical tracer on timescales of a week or so within most of the lower](#)
11 [stratosphere \(Heese et al., 2001\). The MIMOSA model can also be used to determine the origin](#)
12 [of air masses influencing a given site, similar to an isentropic Lagrangian trajectory model](#)
13 [\(Bencherif et al., 2011; Hauchecorne et al., 2002; Portafaix et al., 2003; Bègue et al., 2017\).](#)

Mis en forme : Couleur de police : Texte 1

14 **3. Formation of an intense stratospheric BB plume over Australia**

Mis en forme : Couleur de police : Automatique

15 [Figure 1 shows the AAI obtained from OMPS on board CALIOP over New-Zealand on 1st](#)
16 [January.](#) Following the strongest outbreak during New Year's Eve, a wide plume of BB aerosol
17 with large values of AAI (higher than 12) is transported toward the Tasman Sea on 1st January
18 2020 (Fig. 1a). [Figure 1b depicts the CALIOP attenuated scattering ratio \(SR\) profiles on 1st](#)
19 [January 2020 above New-Zealand.](#) The CALIOP attenuated SR profiles are calculated along the
20 CALIOP track (blue line in Fig. 1a) crossing the absorbing aerosol plume [above New-Zealand.](#)
21 CALIOP observations reveal a broad region of high values (ranging from 10 to 25) between
22 36° S and 46°S centered at 16.5 km altitude (Fig. 1b).

23 Figure 2a illustrates the daily extinction profiles at 532 nm derived from lidar measurements
24 over Lauder (New-Zealand) between 1st December 2019 and 1st April 2020. Note that a strong
25 convective activity prevented lidar operations between mid-December 2019 and the 1st January
26 2020. [Figure 2a reveals high values in the extinction \(from \$3 \times 10^{-3} \text{ km}^{-1}\$ to \$9 \times 10^{-3} \text{ km}^{-1}\$ \) in the](#)
27 [stratosphere over Lauder starting in mid-January 2020, one order of magnitude above the](#)
28 [typical stratospheric aerosol background \(Sakai et al., 2016\).](#) [Figure 2a reveals a sharp increase](#)
29 [in the extinction in the stratosphere over Lauder starting from mid January 2020 with values](#)
30 [ranging from \$3 \times 10^{-3} \text{ km}^{-1}\$ to \$9 \times 10^{-3} \text{ km}^{-1}\$, one order of magnitude above the typical](#)
31 [stratospheric aerosol background \(Vernier et al., 2012\).](#) The vertical extent of the plume
32 increased significantly between mid-January and 1st April 2020 with an aerosol layer spanning
33 from 11.5 to 20 km. [The ascent of the aerosol plume could be attributed to efficient adiabatic](#)

1 heating as a result of the strong absorption of solar radiation by this black carbon rich plume.
2 The ascent of BB aerosol could be due to adiabatic heating effect (De Laat et al., 2012). A
3 statistically significant increase of sAOD (between 15 and 30 km) is observed in January 2020
4 (2.5 times higher than background value) and still visible in April 2020 with same amplitude
5 (Fig. 2b).

6 Figure 2b depicts the daily evolution of CO mixing ratio profile obtained from FTIR
7 measurements over Lauder between 1st December 2019 and 1st April 2020. The same observation
8 can be made for the carbon monoxide in the UTLS over New-Zealand, as shown in Figure 3
9 with the observations made by the FTIR at Lauder. Prior to the convective period, the maximum
10 of CO mixing ratio (120-130 ppbv) is observed in the troposphere (Fig. 3a). An increase of CO
11 mixing ratio in the lower stratosphere is visible from mid-December 2019 with the maximum
12 (50-90 ppbv) observed in the UT-LS (9-13 km). The partial column of CO (between 9 and 30
13 km), calculated from FTIR, reaches its maximum values (~33 % higher than background value)
14 in January 2020 and slightly decreases in April 2020 (~24% higher than background value)
15 (Fig. 3b). Above the lower stratosphere, the CO mixing ratio decreases significantly due to
16 photochemical reactions which are more efficient with altitude (Brasseur and Solomon, 2005).
17 An increase of CO mixing ratio in the lower stratosphere is visible from mid-December 2019.
18 One can observe that the maximum of the CO mixing ratio (50-90 ppbv) is mainly observed in
19 the UT-LS (9-13 km) during the February-April 2020 period. This could be explained by the
20 fact that CO decays quickly due to photochemical oxidation whose efficiency increase with
21 altitude.

22 The injection of BB aerosols and CO in the stratosphere induced significant disturbance evident
23 in the total columns over Lauder (Fig. 3a). Figure 3a depicts the monthly mean evolution of
24 AOD and total columns of CO (TCO) at Lauder between 1st December 2019 and 1st April 2020
25 obtained from sky radiometer and FTIR measurements, respectively. AOD reaches its
26 maximum value (0.17, 3 times higher than background value) in January 2020, decreasing to
27 background values in February 2020 (Fig. 3a). The similar evolution is also observed for the
28 TCO values. An abrupt increase in TCO (~9 % of the pre-event levels) is observed in January
29 2020 and the return to pre-event values is observed as of February 2020 as also already shown
30 in Kloss et al. (2021). Conversely, the perturbation on the stratospheric columns still persisting
31 after February 2020. Figure 3b illustrates the monthly mean evolution of stratospheric AOD
32 (sAOD) and CO (sCO) columns at Lauder between 1st December 2019 and 1st April 2020. The
33 sAOD and sCO are calculated between 12 and 30 km from lidar and FTIR measurements,
34 respectively. The evolution of sAOD and sCO is fairly similar (Fig. 3b). A statistically

Mis en forme : Police :Non Gras, Couleur de police :
Automatique

1 significant increase of sAOD is observed in January 2020 (2.5 times higher than background
2 value) and still visible in April 2020 with same amplitude. sCO reaches its maximum values
3 (-24 % of the pre-event levels) in January 2020 and slightly decreases in April 2020 (-14% of
4 the pre-event).

5 Our works suggest that the injection of CO and absorbent aerosols ends up de-correlated in
6 space and altitude given their different properties. In order to extend the discussion, the spatial
7 dispersion of the Australian BB plume in the Southern Hemisphere will be discussed in the next
8 section.

9 **4. Transport Presence of the Australian BB plume over the SWIO** 10 **basin**

11 **4.1 Aerosol and CO variability over a subtropical site: Reunion**

12 ~~Figure 4 depicts a time-averaged map of partial columns of aerosols (between 15 and 30 km,~~
13 ~~sAOD) and CO (between 9 and 30 km) obtained from OMPS and IASI observations between~~
14 ~~9th and 16th January 2020, respectively.~~ ~~Figure 4 shows time-averaged maps for AOD from~~
15 ~~OMPS and CO partial column (9-30 km) from IASI observation.~~ The transport of the aerosol
16 (with values ranging from 6×10^{-3} to 1×10^{-2} km⁻¹) and CO (with values ranging from 6 to $8 \times$
17 10^{17} molecules. cm⁻²) plume over the Southern Pacific occurred mainly within the 18°S–60°S
18 latitudinal band. One can observe an aerosol band (with values ranging from 5×10^{-3} to $9 \times 10^{-$
19 3 km⁻¹) across the Southern Hemisphere between 40°S and 60°S during the 9-16th January 2020
20 period (Figure 4a). The Australian aerosol plume has already circled the Southern Hemisphere
21 during the first two weeks of January 2020. The same conclusion cannot be made for CO from
22 space-borne observations (Figure 4b). One can observe weak values of CO (less than 5×10^{17}
23 molecule.cm⁻²) over southern Atlantic and without a real link with the large plume observed
24 over southern Pacific (Fig. 4b).

25 Figure 5a depicts the evolution of the sAOD at 532 nm calculated between 15 and 30 km from
26 the ground-based lidars (~~LiO3T and LiO3S~~) and OMPS observations over Reunion from 1st
27 January to 1st March 2020. ~~OMPS extinctions are converted to 532 nm using an Angström~~
28 ~~exponent for the 532–745 nm wavelength pair of 1.9, as prescribed by Taha et al. (2021).~~ ~~The~~
29 ~~Angström exponent for the 532–745 nm wavelength pair is adopted from methodology in Taha~~
30 ~~et al. (2021) and set to 1.9. Lidar observations over Reunion are also used to calculate the~~
31 ~~aerosol Angstrom exponent (using 355 nm and 532 nm pairs).~~ ~~Reunion witnessed An~~ abrupt
32 increase in the aerosol loading (~~three times above the typical background~~) is clearly observed
33 ~~over Reunion~~ as of 16th January 2020 according to satellite observations. ~~This increase of the~~
34 ~~aerosol loading, three times above the typical background, was still visible until 1st March 2020.~~

Mis en forme : Couleur de police : Automatique

Mis en forme : Police : Non Gras, Couleur de police : Automatique

Mis en forme : Police : Non Gras, Couleur de police : Automatique

Mis en forme : Couleur de police : Automatique

Mis en forme : Police : Non Gras, Couleur de police : Automatique

Mis en forme : Police : Non Gras, Couleur de police : Automatique

Mis en forme : Police : Non Gras, Couleur de police : Automatique

~~It is worthwhile mentioning that~~ The sAOD values observed between 16th January and 1st March 2020 are higher than those observed during the passage of the Calbuco plume over Reunion site, which did not exceed 0.013 (Bègue et al., 2017). The increase of sAOD in mid-January coincided with an increase of CO, as shown in Figure 5b based on the use of partial columns (between 9 and 30 km) and CO abundance from IASI and FTIR at the same site and over the same period. ~~The evolution of CO obtained from IASI and FTIR measurements correlate.~~ The ground-based observations show that the CO abundance observed during this increased phase is on average 20% higher than the values observed during the background period (Fig. 5b). ~~The evolution of sAOD and CO observations in mid-January suggests that Reunion, and its surrounding, have been influenced by the transport of the Australian BB plume. The evolution of sAOD and CO observations in mid-January suggests that Reunion, and its surrounding, have been influenced by the transport of the BB plume.~~

Figures 6a and 6b illustrate the night-averaged extinction profiles at 355 nm derived from lidar measurements over Reunion on January and February 2020, respectively. Figure 6 shows aerosol extinction profiles at 355 nm over Reunion for selected days in January or February compared to the January or February background profiles. The two first weeks of January 2020 are representative of the January typical background (shaded area), as illustrated on 13th January 2020 (Fig. 6a). Conversely, the extinction profiles at the end of January 2020 (27th and 28th) are marked by a significant increase (4 times higher than the background values) located in the lower stratosphere between 16.8 and 18 km altitude (equivalent to potential temperature levels 380-404 K). ~~One can observe that the structure of the extinction profile in the lower stratosphere has changed between these two days.~~ On 28th January, the extinction profile exhibits a sudden increase at 17.4 km (~400 K) and quickly decreased afterwards to values observed the previous day (Fig. 6a). ~~It is worthwhile mentioning that~~ The values of extinction (10 to $17 \times 10^{-3} \text{ km}^{-1}$) observed in the lower stratosphere on these two days are of the same order as those observed at Lauder a few days after the pyro-convective event (Fig. 2). ~~Figure 6a also reveals a statistically significant increase (4 times higher than background values) in aerosol extinction between 15 and 16.5 km altitude (361-375 K), on 27th and 28th January 2020. Over Reunion, the lidar observations hence confirm the presence of a significant aerosol layer in the UT-LS by the end of January.~~ In February, the extinction profiles clearly exhibit two significant aerosol layers with the first one located between 16 and 19.5 km (370-440 K) and the second one between 20 and 22.5 km (465-500 K) (Fig. 6b).

To further discuss the optical properties of these aerosol layers, the Angström exponent has been calculated between 355 nm and 532 nm from the ~~ground-based lidar LiO3S and LiO3T~~

Mis en forme : Police :Non Italique

Mis en forme : Police :Non Gras, Couleur de police : Automatique

1 measurements (Figs. 6c and 6d). In February, the Angström exponent values reveal that the two
2 aerosol layers consist mainly of small aerosol particles (Fig. 6d), consistent with a stratospheric
3 smoke layer (Haarig et al., 2018; Hu et al., 2019; Ohneiser et al., 2021). In January, the profile
4 of Angström exponent exhibits more variability in the UT-LS (Fig. 6c) with values ranging
5 from 0.6 to 1.9, on 27th and 28th January. ~~Based on the literature, the largest proportion of the
6 observed Angström exponent range (up to ~1.5) within the plume, points to the presence of an
7 aerosol layer (Das et al., 2021; Haarig et al., 2018; Hu et al., 2019; Kloss et al., 2019).~~ The wide
8 range of Angström exponent values suggests that the aerosol layer is not homogeneously
9 distributed at this stage and might be interpreted as a mixture of fresh and aged smoke layers
10 (Fig. 6c). ~~Indeed, Müller et al, 2007 showed that ageing of transported smoke translates into a
11 decreasing of the Angström exponent. This may indicate growth and removal processes (e.g.,
12 coagulation, condensation, sedimentation) which can modulate the morphology and mixing
13 state of the aerosol layer during its transport (Burton et al., 2015; Hamil et al., 1997). The
14 residence time of the aerosol particles in the atmosphere depends on the balance between the
15 growth processes and the removal processes, which are likely to be controlled by the dynamical
16 context. Previous works showed that the dynamical context can modulate the structure and
17 optical properties of the aerosol layer over a given site from day to day (Bègue et al., 2017;
18 Kremser et al., 2016). Fresh aerosols can be rapidly transported and mixed with pre-existing
19 aged aerosols.~~ Given the fact that the Angström exponent values decrease with the duration of
20 transport, we cannot exclude that the vertical distribution of optical properties of aerosol over
21 Reunion may also be explained by the regional transport of air masses.

22 4.2 Origin of the air masses

23 To analyze the origin of air masses at Reunion on 27th and 28th January, one-month backward
24 trajectories were calculated using FLEXPART (Aliaga et al., 2021; Eckhardt et al., 2017; Xu
25 et al., 2021). A period of one month was chosen because it refers to the time lapse separating
26 the pyro-convective outbreak event and the day of the measurement at Reunion. The
27 representation of the ~~PES~~ (potential emission sensitivity) (PES) from back-trajectories
28 simulations initialized at 18 km originating from Reunion on 27th and 28th January 2020 are
29 presented in Figure 7.

30 Figures 7A-1 and 7B-1 display the horizontal trajectories, whereas vertical movement is shown
31 in Figures 7A-2 and 7B-2, respectively. The vertical transect of FLEXPART back trajectories
32 in Figure 7A-2 confirms a high probability of air mass contribution from Australia if the fires
33 emissions are directly injected into the stratosphere by convection (black rectangle in the
34 figure), (i.e. layer of 9 to 16 km of injection taken for the PES, see section 2.3.1). ~~Then,~~

Mis en forme : Police :Non Gras, Couleur de police :
Automatique

Mis en forme : Couleur de police : Automatique

Mis en forme : Police :Non Gras, Couleur de police :
Automatique

Mis en forme : Police :Non Gras, Couleur de police :
Automatique

Mis en forme : Couleur de police : Automatique

1 ~~a~~According to FLEXPART results, ~~the air masses at 18 km over Australia moved westward~~
2 ~~and reached Reunion on 27th January. One can observe that the same pattern is observed on 28th~~
3 ~~January 2020 (Figs. 7B-1 and 7B-2). One part of the Australian smoke layer is advected zonally~~
4 ~~by the prevailing easterly winds and is observed over Reunion on 27th and 28th January 2020 at~~
5 ~~18 km. It is worth mentioning that the same pattern has been observed during the volcanic~~
6 ~~eruption of the Hunga Tonga on January 2022 (Baron et al., 2023, Kloss et al., 2022; Sellitto et~~
7 ~~al., 2022). The FLEXPART simulations also suggest that Reunion is also influenced by~~
8 ~~eastward transport of air masses. This pathway is clearly visible on 28th January 2020 (Figs.~~
9 ~~7B-1 and 7B-2). Figure 7B-1 reveals that air masses coming from the South American region~~
10 ~~and Australia region both reach the SWIO basin by passing over southern Africa. Furthermore,~~
11 ~~a~~Air masses from high latitudes seem to cross the subtropical latitudes following a wave shape
12 and reach the SWIO basin by passing over the Cape of Good Hope (Figure 7B-1).

13 In order to ~~delve further improve the discussion~~ on this eastward transport of air masses over
14 the SWIO basin, the MIMOSA model has been used to produce a continuous evolution of PV
15 fields for the period from 1st to 31st January 2020 ~~for the 400 K isentropic level. Two advected~~
16 ~~PV maps derived for the 400 K isentropic level from the MIMOSA model are depicted in Figure~~
17 ~~8.~~The localization of the aerosol plume obtained from OMPS observations at the $400 \text{ K} \pm 5 \text{ K}$
18 isentropic level are also superimposed (Fig. 8). The 400 K isentropic level is chosen according
19 to the layers observed in the extinction profiles over Reunion between 390 and 404 K isentropic
20 level on 27th and 28th January 2020 (Fig. 6a). ~~Figure 8 reveals significant wave activity during~~
21 ~~these two days. It is clearly shown that a~~Air masses from mid-latitudes ($40\text{-}60^\circ\text{S}$) cross the
22 subtropical latitudes ($20\text{-}40^\circ\text{S}$) and are advected eastward between South Africa and
23 Madagascar following a wave shape (Fig. 8). Given the Australian BB aerosol are mainly
24 located in the mid-latitudes (Fig. 4a), we can reasonably conclude that the filament reaching
25 the SWIO basin contains aerosol from the Australian BB event. On 27th January, air masses
26 containing aerosol are observed at Madagascar and its surroundings (Fig. 8a). These air masses
27 are advected eastward ~~following the displacement of the wave shape~~and reach Reunion on 28th
28 January (Fig. 8b). ~~Parts of the smoke plume underwent an isentropic transport from the mid to~~
29 ~~tropical latitudes. following two distinct pathways to reach Reunion.~~

30 Our analysis ~~demonstrated suggests~~ that the Australian BB plume was transported over the
31 SWIO basin following two distinct pathways. ~~To extend to which Australian BB plume has~~
32 ~~contributed to the variability of the atmospheric compound over the SWIO basin is now~~
33 ~~investigated.~~

Mis en forme : Police :Non Gras, Couleur de police :
Automatique

Mis en forme : Police :Non Gras, Couleur de police :
Automatique

4.3 Contribution Influence of the Australian BB plume on the CO and aerosol variability

Because a significant simultaneous increase of CO and sAOD is observed over Reunion and its surroundings from 16th to 29th January 2020, the investigation will focus on this period. The emission sensitivity from FLEXPART, at the altitude where the emissions are injected is combined with CO and aerosol (BC and OC) emission inventory. The CO emissions due to anthropogenic activity are also taken into account considered by coupling the FLEXPART model with the EDGAR inventory information. Figure 9 depicts the evolution of the sAOD and the partial column of CO (between 9 and 30 km) obtained from satellites observations and simulated by FLEXPART from 15th to 29th January over Reunion. Unfortunately, few data have been recorded during the period aforementioned. Nevertheless, the simulated sAOD and partial column of CO compare fairly well with the available satellite observations during this period, and the peak observed on mid-January is acceptably well reproduced. The simulated sAOD compare fairly well with the available satellite observations during the 15-29 January period, and the peak observed on mid-January is acceptably well reproduced. Conversely, the partial column of CO seems less consistent with the observations made by IASI.

The discrepancies between FLEXPART and observations may be attributable to several possible caveats. One of which possible source of error can be the lack of fact that the vertical motion induced by pyro-convection is not included in FLEXPART. We tested this issue by applying an injection height in agreement with CALIOP observations (9-16 km, Fig. 1) for the Australian plume (Khaykin et al., 2020). The injection height of the plume plays a key role in its long-range transport (Sofiev et al., 2012). An inappropriate or unrealistic injection height can lead to either a dilution or an overestimation of the plume. The injection height depends on the intensity of the fire, as well as on the meteorological conditions. Another possible explanation in these differences can come from the duration of the backward calculation (1 month) and an underestimation of the emission by GFAS (Brocchi et al., 2018). The discrepancies may also be the result of an underestimation of the emissions by GFAS. In the framework of their FLEXPART simulation Using FLEXPART simulations, Brocchi et al. (2018) reveal that an amplification factor of two has been applied to CO emissions from GFAS to obtain comparable get similar CO quantities with observations. The other source of difference between the model and the observations stems mainly from whether or not FLEXPART takes several regions into account as a source of pollution. The results shown in the figure 9 target emissions from Australia only. The contribution of other regions is discussed in section 5.

Mis en forme : Couleur de police : Automatique

Mis en forme : Police : Non Gras, Couleur de police : Automatique

Mis en forme : Police : Non Gras, Couleur de police : Automatique

Mis en forme : Police : Non Gras, Couleur de police : Automatique

Mis en forme : Police : Non Gras, Couleur de police : Automatique

Mis en forme : Police : Non Gras, Couleur de police : Automatique

Mis en forme : Police : Non Gras, Couleur de police : Automatique

Mis en forme : Police : Non Gras, Couleur de police : Automatique

Mis en forme : Police : Non Gras, Couleur de police : Automatique

Mis en forme : Police : Non Gras, Couleur de police : Automatique

On average, the aerosol emissions from Australia contributed up to 95 % of the sAOD variability over Reunion from 15th to 29th January (Fig. 9a). Conversely, the CO emissions from Australia ~~fire~~ contribute up to 10% of the enhancement of the partial column of CO from 15th to 29th January (Fig. 9b). ~~Therefore, t~~The transport of the CO plume induced by the Australian sources has not been efficiently ~~transported~~ over the SWIO basin. ~~The variability of CO over the SWIO basin could be mainly explained by the regional transport of air masses. Therefore, our analysis suggests that t~~The variability of CO over the SWIO basin in January is ~~therefore not significantly driven by emissions from Australian fires. could be explained both~~ by long range and regional transport of air masses. The extent to which regional sources have contributed to the variability of the CO and aerosol over the SWIO is now investigated.

5. Discussion on the influence of the regional sources

~~The representation of the PES from back trajectories simulations initialized at 16 km originating from Reunion for the 27th and 28th January 2020 are presented in Figure 10. Figure 10A-1 and 10B-1 reveal that the trajectories from Reunion at 16 km pass over southern Africa and Madagascar. One can observe that the highest values of PES are located over southern Africa and Madagascar (Figs. 10A-1 and 10B-1). Furthermore, the FLEXPART simulations suggest that air masses from southern Africa and Madagascar might have reached altitudes up to 16 km between 25[°]E and 55[°]E in longitude and reached Reunion on 27th and 28th January 2020 (Figs. 10A-2 and 10A-2). The results of Figure 10 show an influence of air masses coming from Africa and reaching the SWIO basin at 16 km. Thus, the moderate increase in aerosol extinction observed in the upper troposphere (between 16 and 17 km altitude) on 27th and 28th January in Figure 6a may be attributed to air masses from regional sources, namely southern Africa and Madagascar.~~

~~The location of fire flagged pixels and the associated Fire Radiation Power (FRP) values from MODIS between 16th and 29th January 2020 are reported in Figure 11a. Fire Radiation Power (FRP) gives quantitative information on combustion rates and its intensity (Fig. 10a). The sparse activity of the African fires in January is clearly illustrated in Figure 11a with moderate values of FRP ranging from 20 to 200 MW.m⁻². These values are ten times lower than those observed over the southeastern Australia between 30th December 2019 and 12th January 2020 (Bègue et al., 2021). ~~One can observe that the~~The off-season African BB activity in January 2020 is mainly located over the northwestern (near the Equator) and southeastern side of southern Africa. The most intense values (100-200 MW.m⁻²) are observed over the southeastern side.~~

Mis en forme : Police :Non Gras, Couleur de police : Automatique

Mis en forme : Police :Non Gras, Couleur de police : Automatique

Mis en forme : Police :Non Gras, Couleur de police : Automatique

Mis en forme : Police :Non Gras, Couleur de police : Automatique

Mis en forme : Police :Non Gras, Couleur de police : Automatique

Mis en forme : Police :Non Gras, Couleur de police : Automatique

Mis en forme : Couleur de police : Automatique

Mis en forme : Police :Non Gras, Couleur de police : Automatique

Mis en forme : Couleur de police : Automatique

Mis en forme : Police :Non Gras

Mis en forme : Police :Non Gras, Couleur de police : Automatique

Mis en forme : Police :Non Gras, Couleur de police : Automatique

Mis en forme : Police :Non Gras, Couleur de police : Automatique

Mis en forme : Police :Non Gras, Couleur de police : Automatique

Mis en forme : Police :Non Gras, Couleur de police : Automatique

Mis en forme : Police :Non Gras, Couleur de police : Automatique

1 ~~To further discuss the vertical distribution of CO in the UT LS within the region of deep~~
2 ~~convection, † To further investigate the convection driven pathway, †~~ the vertical cross section of
3 CO and water vapor mixing ratio anomalies calculated from MLS observations between 16th to
4 29th January 2020 are analyzed (Figs. 112a and 112b). The CO and water vapor mixing ratio
5 anomalies are calculated as a relative difference by considering the monthly background means
6 as the reference values. The calculations are performed over a domain extending between 10°S
7 and 25°S in latitude and 30°E and 60°E in longitude (black box in Fig. 104b). ~~The altitude-~~
8 ~~longitude cross section is averaged for all latitudes covering the study domain.~~ This domain
9 includes both the region of deep convection and the first region of high values of CO. The
10 monthly background is calculated from available MLS observations in January between 2017
11 and 2019. Figure 12a exhibits two regions of high values of CO mixing ratio anomalies (higher
12 than 15%) centered at 37°E and 50°E in longitude ~~at 146 hPa (~15 km) and 100 hPa (~17 km).~~
13 ~~The maximum CO mixing ratio anomalies in the first region are centered at 215 hPa (~12 km)~~
14 ~~with anomalies ranging from 25% to 30%. The values of the anomalies decreased rapidly with~~
15 ~~altitude. Indeed, the anomalies values obtained at 146 hPa (~15 km) and 100 hPa (~17 km)~~
16 ~~ranged from 20% to 25% and from 15% to 20%, respectively. In the second region, the~~
17 ~~maximum CO mixing ratio anomalies are also centered in the middle troposphere (215 hPa).~~
18 ~~One can observe that †~~ These regions of CO mixing ratio anomalies are † in coincidence with two
19 regions of high values (higher than 20%) of water vapor mixing anomalies (Fig. 112b). ~~The~~
20 ~~maxima of water vapor mixing ratio anomalies are centered at 146 hPa with values ranging~~
21 ~~from 40% to 50%. This is consistent with the FLEXPART simulations shown in figure 12 which~~
22 ~~highlight a lift of air masses from the lower troposphere to lower stratosphere between 25°E to~~
23 ~~55° E in longitude. † We can assume that †~~ the convective activity induced by Diane near
24 Madagascar may have contributed to lift air masses enriched in CO from the lower troposphere.
25 ~~This is consistent with the FLEXPART simulations which highlight a lift of air masses from~~
26 ~~the lower troposphere to lower stratosphere between 25°E to 55° E in longitude (Figure 9). One~~
27 ~~can observe that the most significant anomalies of the vertical distribution of CO and water~~
28 ~~vapor mixing ratio stretch from the middle troposphere (215 hPa) up to the tropopause layer~~
29 ~~(100 hPa.). At 68 hPa, it can be observed that high values of water vapor mixing ratio anomalies~~
30 ~~are not in coincidence with high values of CO mixing ratio anomalies, but located along the~~
31 ~~vertical extent of the maxima of CO mixing ratio anomalies in the troposphere.~~
32 ~~Our analysis corroborates the results found by Héron et al. (2020). Based on radiosonde and~~
33 ~~satellite observations, Héron et al. (2020) showed that convective activity over the SWIO basin~~
34 ~~has the potential to influence the variability of ozone and water vapor in the upper troposphere~~

Mis en forme : Police :Non Gras, Couleur de police : Automatique

Mis en forme : Police :Non Gras, Couleur de police : Automatique

Mis en forme : Police :Non Gras, Couleur de police : Automatique

Mis en forme : Police :Non Gras, Couleur de police : Automatique

Mis en forme : Police :Non Gras, Couleur de police : Automatique

Mis en forme : Police :Non Gras, Couleur de police : Automatique

Mis en forme : Police :Non Gras, Couleur de police : Automatique

Mis en forme : Police :Non Gras, Couleur de police : Automatique

Mis en forme : Police :Non Gras, Couleur de police : Automatique

Mis en forme : Police :Non Gras, Couleur de police : Automatique, Anglais (États-Unis)

Mis en forme : Police :Non Gras, Couleur de police : Automatique

1 during the austral summer. Our results demonstrate that the variability of CO and aerosol over
2 the SWIO basin can be explained both by the influence of long range transport of the Australian
3 fires plumes, together with regional transport from southern Africa, enhanced by convective
4 activity due to the passage of a tropical storm.

5 Figure 9 also depicts the evolution of the contribution of the African emission on CO₂ and
6 ~~and~~ partial columns, obtained from satellites observations and simulated by FLEXPART from
7 15th to 29th January over Reunion. An injection height ranging up to 3 km was chosen for the
8 African fires (Labonne et al., 2007). The Australia contribution on the observed partial column
9 was plotted again (as from figure 9). On average, the CO emissions from Africa contribute up
10 to 90% of the enhancement of the ~~total and~~ partial column of CO from 15th to 29th January (Fig.
11 139b). The total Africa and Australia CO contribution reproduce fairly well the observations.
12 Conversely, the evolution of sAOD is not correlated to the evolution of the aerosol emission
13 from Africa, which is marked by an increase from 21st to 29th January. The weak contribution
14 of African component on the sAOD can be explained by the fact that the amounts of African
15 BB aerosols injected in the atmosphere by the convective activity decrease with altitude.
16 Moreover, it is likely that aerosol would be scavenged by cloud droplets (a process taken into
17 account in FLEXPART) in a strongly convective environment such as tropical storm Diane.

18 Our results ~~suggest~~ demonstrate that the variability of CO ~~and aerosol~~ over the SWIO basin can
19 be explained both by the influence of ~~the long range transport of the Australian fires plumes,~~
20 ~~together with~~ regional transport from southern Africa, enhanced by convective activity due to
21 the passage of a tropical storm.

22 6. Summary and Conclusion

23 The complex aerosol and CO variabilities over the SWIO basin during the 2020 austral summer
24 have been investigated. The meteorological context and the extensive fires over southeastern
25 Australia were favorable for triggering pyro-convective events between 29th December 2019
26 and 12th January 2020. These pyro-convective events led to a massive injection of combustion
27 products in the stratosphere. The ground-based and space-borne lidars revealed the presence of
28 an intense stratospheric aerosol layer over the southeastern Australia region. Over the Lauder
29 site in New-Zealand, this smoke layer was detected into the stratosphere (centered at 16 km)
30 until April and beyond. The analysis of the spatial and temporal dispersion of the Australian
31 BB plume highlighted its quick transport circling the entire Southern Hemisphere in less than
32 two weeks. Furthermore, the satellite observations revealed that the transport of the Australian
33 smoke layer was mainly bounded within an extra-tropical latitudinal band.

Mis en forme : Police :Non Gras, Couleur de police :
Automatique

Mis en forme : Police :Non Gras, Couleur de police :
Automatique

Mis en forme : Police :Non Gras, Couleur de police :
Automatique

Mis en forme : Police :Non Gras, Couleur de police :
Automatique

Mis en forme : Police :Non Gras, Couleur de police :
Automatique

Mis en forme : Police :Non Gras, Couleur de police :
Automatique

Mis en forme : Police :Non Gras, Couleur de police :
Automatique

1 Nevertheless, the numerical models clearly showed the influence of the Australian smoke layer
2 on the variability of aerosol over the SWIO basin. Over Reunion, the aerosol extinction profiles
3 exhibited a significant increase in the lower stratosphere during the end of January. The
4 MIMOSA simulations highlighted the isentropic transport of the Australian BB aerosol from
5 extra-tropical latitudes to Reunion at 400 K isentropic level, on 28th January. As a consequence,
6 the corresponding aerosol extinction profile exhibited a sudden increase by drawing a structure
7 similar to a laminae at the 400 K isentropic level. The aerosol extinction profiles also exhibited
8 a moderate increase in the upper troposphere.

9 ~~According to our simulations, the CO variability over the SWIO cannot be explained by the~~
10 ~~Australian Black Summer. Rather, the CO in the UT-LS is likely driven by African BB~~
11 ~~emissions during the convective season.~~

12 ~~This paper investigates for the first time the possibility of the African emissions from BB to~~
13 ~~influence the CO and aerosol distribution in the UT-LS during the convective season. Despite~~
14 ~~the fact that African BB activity is usually sparse in January, it contributed to modulation of the~~
15 ~~vertical distribution of CO and aerosols in the upper troposphere over the SWIO basin. The~~
16 analysis of satellite observations and FLEXPART simulations suggests that, because of the
17 convective activity, air masses enriched in CO and aerosols have been lifted from the lower
18 troposphere to the lower stratosphere. Air masses from Africa contributed up to 90% of the total
19 and partial column (between 9 and 30 km) of CO variability over Reunion and its surroundings.
20 The simulations shows that the modulation of the CO and aerosol extinction in the upper
21 troposphere and the lower stratosphere over Reunion was driven by the transport of air masses
22 from both Africa and Australia, respectively. ~~Our findings suggest simultaneous presence of~~
23 ~~African and Australian aerosol smoke layers at Reunion.~~

24 Acknowledgements

25 Data used in this publication were obtained from NDACC network and are available through
26 its website (<http://www.ndacc.org/>). The work of S. Khaykin has been supported by the Agence
27 Nationale de la Recherche PyroStrat project (21-CE01- 335 0007-01). IASI was developed and
28 built under the responsibility of the “Centre National d’Etudes Spatiales” (CNES, France) and
29 flown on board the MetOp satellites as part of the EUMETSAT Polar System. The authors
30 thank the AERIS infrastructure (<https://iasi.aeris-data.fr/>) for providing access to the IASI data,
31 the National Aeronautical and Space Administration (NASA) for providing CALIOP data,
32 MLS and MODIS fire products. We would especially like to thank the staff of the team working
33 on the lidar systems at the Maïdo observatory. The French Research Infrastructure ACTRIS-
34 FR, CNES are also acknowledged for their support in the upgrade and operation of the Maïdo

Mis en forme : Couleur de police : Automatique

Mis en forme : Espace Après : 0 pt

Mis en forme : Police : Non Gras, Couleur de police : Automatique

Mis en forme : Couleur de police : Automatique

Mis en forme : Police : Non Gras, Couleur de police : Automatique

Mis en forme : Police : Non Gras, Couleur de police : Automatique

Code de champ modifié

Code de champ modifié

1 observatory lidars. Lauder observations are funded by the New-Zealand Government's Strategic
2 Science Investment Fund (SSIF), administered by the Ministry of Business, Innovation and
3 Employment (MBIE). The TCCON site at Réunion Island has been operated by the Royal
4 Belgian Institute for Space Aeronomy with financial support since 2014 by the EU project
5 ICOS-Inwire, the ministerial decree for ICOS (FR/35/IC1 to FR/35/C6), ESFRI-FED ICOS-
6 BE project and local activities supported by LACy/UMR8105 and by OSU-R/UMS3365 –
7 Université de La Réunion. The lidar measurements at Lauder are supported by funding from
8 GOSAT series project.

9 **Data availability**

10 The data used for this study are available and open access by request to scientist mentioned or
11 through the link hereafter: Lidar measurements (tetsu@mri-jma.go.jp, [nelson.begue@univ-
12 reunion.fr](mailto:nelson.begue@univ-reunion.fr)), FTIR measurements from TCCON network (mahesh.sha@aeronomie.be); Lauder
13 FTIR data available on the NDACC public access database ([https://www-
14 air.larc.nasa.gov/missions/ndacc/data.html](https://www-air.larc.nasa.gov/missions/ndacc/data.html)); The satellite observations and emission inventory
15 used are available on-line from the sources as stated in the manuscript. [The FLEXPART and
16 MIMOSA codes are available on the FLEXPART \(https://www.flexpart.eu/\) and AERIS
17 website \(http://espri.aeris-data.fr/\), respectively.](https://www.flexpart.eu/)

18 **Authors contributions**

19 Conceptualization, N.B.; methodology and software, N.B, A.B. and G.K.; validation and data
20 curation, N.B., A.B, GK., S.K, C.C., P.C., D.S., J.R., R.Q, B.R, S.T and P.S.; original draft
21 preparation and writing, N.B.; [The FLEXPART and MIMOSA simulations have been
22 performed by GK and NB. respectively.](#) All authors have read and agreed to the published
23 version of the manuscript.

Code de champ modifié

Code de champ modifié

Code de champ modifié

Mis en forme : Police :Non Gras

Mis en forme : Police :Non Gras

1 REFERENCES

- 2 Aliaga, D., Sinclair, V. A., Andrade, M., Artaxo, P., Carbone, S., Kadantsev, E and Bianchi,
3 F.: Identifying source regions of air masses sampled at the tropical high-altitude site of
4 Chacaltaya using WRF-FLEXPART and cluster analysis. *Atmospheric Chemistry and Physics*,
5 21(21), 16453-16477, 2021
- 6 Andreae, M. O and Merlet, P.: Emission of trace gases and aerosols from biomass burning.
7 *Global biogeochemical cycles*, 15(4), 955-966, 2001
- 8 [Atkinson, R., Baulch, D. L., Cox, R. A., Crowley, J. N., Hampson, R. F., Hynes, R. G., Jenkin,](#)
9 [M. E., Rossi, M. J., Troe, J., and IUPAC Subcommittee: Evaluated kinetic and photochemical](#)
10 [data for atmospheric chemistry: Volume II – gas phase reactions of organic species, *Atmos.*](#)
11 [Chem. Phys., 6, 3625–4055, <https://doi.org/10.5194/acp-6-3625-2006>, 2006.](#)
- 12 [Baray, J.-L., Courcoux, Y., Keckhut, P., Portafaix, T., Tulet, P., Cammas, J.-P., Hauchecorne,](#)
13 [A., Godin Beekmann, S., De Mazière, M., Hermans, C., Desmet, F., Sellegri, K., Colomb, A.,](#)
14 [Ramonet, M., Sciare, J., Vuillemin, C., Hoareau, C., Dionisi, D., Duflot, V., Vèrèmes, H.,](#)
15 [Porteneuve, J., Gabarrot, F., Gaudo, T., Metzger, J.-M., Payen, G., Leclair de Bellevue, J.,](#)
16 [Barthe, C., Posny, F., Ricaud, P., Abchiche, A., and Delmas, R.: Maïdo observatory: a new](#)
17 [high-altitude station facility at Reunion Island \(21° S, 55° E\) for long-term atmospheric remote](#)
18 [sensing and in situ measurements, *Atmos. Meas. Tech.*, 6, 2865–2877,](#)
19 [https://doi.org/10.5194/amt-6-2865-2013](#), 2013
- 20 [Baray, J.-L., Leveau, J., Baldy, S., Jouzel, J., Keckhut, P., Bergametti, G., Ancellet, G.,](#)
21 [Bencherif, H., Cadet, B., Carleer, M., David, C., De Mazière, M., Faduïlle, D., Godin-](#)
22 [Beekmann, S., Goloub, P., Goutail, F., Metzger, J.-M., Morel, B., Pommereau, J.-P.,](#)
23 [Porteneuve, J., Portafaix, T., Posny, F., ROBERT, L., and Van Roozendaël, M.: An](#)
24 [instrumented station for the survey of ozone and climate change in the southern tropics, 8,](#)
25 [1020–1028, <https://doi.org/10.1039/b607762e>, 2006.](#)
- 26 [Barimalala, R., Desbiolles, F., Blamey, R. C., & Reason, C.: Madagascar influence on the South](#)
27 [Indian Ocean Convergence Zone, the Mozambique Channel Trough and southern African](#)
28 [rainfall. *Geophysical Research Letters*, 45, 11,380–11,389. <https://doi.org/10.1029/>](#)
29 [2018GL079964](#), 2018
- 30 [Baron, A., Chazette, P., Khaykin, S., Payen, G., Marquestaut, N., Bègue, N. and Duflot, V.](#)
31 [\(2023\). Early Evolution of the Stratospheric Aerosol Plume Following the 2022 Hunga Tonga-](#)
32

Mis en forme : Police :Non Gras, Couleur de police :
Automatique

1 Hunga Ha'apai Eruption: Lidar Observations From Reunion (21° S, 55° E). Geophysical
2 Research Letters, 50(10), <https://doi.org/10.1029/2022GL101751>, e2022GL101751.

Code de champ modifié

3 Barthe, C., Bousquet, O., Bielli, S., Tulet, P., Pianezze, J., Claeys, M. and Zucule, J.: Impact of
4 tropical cyclones on inhabited areas of the swio basin at present and future horizons. part 2:
5 Modeling component of the research program renovrisk-cyclone. Atmosphere, 12(6), 689,
6 2021

7 Bègue, N., Bencherif, H., Jegou, F., Vérèmes, H., Khaykin, S., Krysztofiak, G., Portafaix, T.,
8 Duflot, V., Baron, A., Berthet, G., Kloss, C., Payen, G., Keckhut, P., Coheur, P-F., Clerbeaux,
9 C., Smale, D., Robinson, J., Querel, R and Smale, P. : Transport and variability of tropospheric
10 ozone over Oceania and southern pacific during the 2019–20 Australian bushfires. Remote
11 Sensing, 13(16), 3092, 2021

12 Bègue, N., Vignelles, D., Berthet, G., Portafaix, T., Payen, G., Jégou, F., Bencherif, H., Jumelet,
13 J., Vernier, J. P., Lurton, T., Renard, J. B., Clarisse, L., Duverger, V., Posny, F., Metzger, J.
14 M., and Godin-Beekmann, S.: Long-range isentropic transport of stratospheric aerosols over
15 Southern Hemisphere following the Calbuco eruption in April 2015, 15019–15036,
16 <https://doi.org/10.5194/acp-17-15019-2017>, 2017.

17 Bencherif, H., Bègue, N., Kirsch Pinheiro, D., Du Preez, D. J., Cadet, J. M., da Silva Lopes, F.
18 J. and Clerbeaux, C.: Investigating the long-range transport of aerosol plumes following the
19 Amazon fires (August 2019): a multi-instrumental approach from ground-based and satellite
20 observations. Remote Sensing, 12(22), 3846, 2020

21 Bencherif, H., El Amraoui, L., Kirgis, G., Leclair De Bellevue, J., Hauchecorne, A., Mzé, N.,
22 Portafaix, T., Pazmino, A., and Goutail, F.: Analysis of a rapid increase of stratospheric ozone
23 during late austral summer 2008 over Kerguelen (49.4° S, 70.3° E), Atmos. Chem. Phys., 11,
24 363–373, <https://doi.org/10.5194/acp-11-363-2011>, 2011

25 Boers, R., A. T. de Laat, D. C. Stein Zweers, and R. J. Dirksen: Lifting potential of solar-heated
26 aerosol layers, Geophys. Res. Lett., 37, L24802, doi:10.1029/2010GL045171, 2010

27 Burton, S.P., Hair, J.W., Kahnert, M., Ferrare, R.A., Hostetler, C.A., Cook, A.L., Harper, D.B.,
28 Berkoff, T.A., Seaman, S.T., Collins, J.E., Fenn, M.A., Rogers, R.R., 2015. Observations of the
29 spectral dependence of linear particle depolarization ratio of aerosols using NASA Langley
30 airborne High Spectral Resolution Lidar. Atmos. Chem. Phys. 15, 13453–13473.
31 <https://doi.org/10.5194/acp-15-13453-2015>

1 Brasseur, G. and Solomon, S: *Aeronomy of the Middle Atmosphere: Chemistry and Physics of*
2 *the Stratosphere and Mesosphere*, 3rd edn, 644, Springer-Verlag, 2005.

3 Cai, D., Abram, N. J., Sharples, J. J. and Perkins-Kirkpatrick, S. E. (2022). Increasing intensity
4 and frequency of cold fronts contributed to Australia's 2019–2020 Black Summer fire
5 disaster. *Environmental Research Letters*, 17(9), 094044.

6 Campanelli, M., Estelles, V., Tomasi, C., Nakajima, T., Malvestuto, V., and Martinez-Lozano,
7 J. A.: Application of the SKYRAD improved Langley plot method for the in-situ calibration of
8 CIMEL sun-sky photometers, *Appl. Optics*, 46, 2688–2702, 2007.

9 Che, H., Shi, G., Uchiyama, A., Yamazaki, A., Chen, H., Goloub, P., and Zhang, X.:
10 Intercomparison between aerosol optical properties by a PREDE skyradiometer and CIMEL
11 sunphotometer over Beijing, China, *Atmos. Chem. Phys.*, 8, 3199–3214, doi:10.5194/acp-8-
12 3199-2008, 2008.

13 Clain, G., Baray, J. L., Delmas, R., Diab, R., Leclair de Bellevue, J., Keckhut, P., Posny, F.,
14 Metzger, J. M., and Cammas, J. P.: Tropospheric ozone climatology at two Southern
15 Hemisphere tropical/subtropical sites, (Reunion Island and Irene, South Africa) from
16 ozonesondes, LIDAR, and in situ aircraft measurements, 9, *Atmos. Chem. Phys.*, 1723–1734,
17 <https://doi.org/10.5194/acp-9-1723-2009>, 2009

18 Clerbaux, C., Boynard, A., Clarisse, L., George, M., Hadji-Lazaro, J., Herbin, H., Hurtmans,
19 D., Pommier, M., Razavi, A., Turquety, S: Monitoring of atmospheric composition using the
20 thermal infrared IASI/MetOp sounder, *Atmos. Chem. Phys.* 2009, 9, 6041–6054, 2009.

21 Coheur, P.-F., Clarisse, L., Turquety, S., Hurtmans, D., and Clerbaux, C.: IASI measurements
22 of reactive trace species in BB plumes, *Atmos. Chem. Phys.*, 9, 5655–5667, doi:10.5194/acp-
23 9-5655-2009, 2009.

24 Darbyshire, E., Morgan, W. T., Allan, J. D., Liu, D., Flynn, M. J., Dorsey, J. R and Coe, H: The
25 vertical distribution of biomass burning pollution over tropical South America from aircraft in
26 situ measurements during SAMBBA. *Atmospheric Chemistry and Physics*, 19(9), 5771-5790,
27 2019

28 De Laat, A.T.J.; Stein Zweers, D.C.; Boers, R.; Tuinder, O.N. A solar escalator: Observational
29 evidence of the self-lifting of smoke and aerosols by absorption of solar radiation in the
30 February 2009 Australian Black Saturday plume. *J. Geophys. Res. Atmos.* 2012, 117.

1 Dowdy, A. J and Pepler, A: Pyroconvection risk in Australia: Climatological changes in
2 atmospheric stability and surface fire weather conditions. *Geophysical Research Letters*, 45,
3 2005–2013. <https://doi.org/10.1002/2017GL076654>, 2018

4 De Mazière, M., Sha, M. K., Desmet, F., Hermans, C., Scolas, F., Kumps, N., Metzger, J.-M.,
5 Dufлот, V., and Cammas, J.-P.: TCOON data from Réunion Island 5RE), Release GG2014.R1,
6 Version R1, CaltechDATA [data set],
7 <https://doi.org/10.14291/TCCON.GGG2014.REUNION01.R1>, 2017

8 Dufлот, V., Dils, B., Baray, J. L., De Mazière, M., Attié, J. L., Vanhaelewyn, G and Delmas, R.:
9 Analysis of the origin of the distribution of CO in the subtropical southern Indian Ocean in
10 2007. *Journal of Geophysical Research: Atmospheres*, 115(D22), 2010

11 ~~Dufлот, V., Royer, P., Chazette, P., Baray, J. L., Coureoux, Y. and Delmas, R.: Marine and BB~~
12 ~~aerosols in the southern Indian Ocean: Retrieval of aerosol optical properties from shipborne~~
13 ~~lidar and Sun photometer measurements. *Journal of Geophysical Research:*~~
14 ~~*Atmospheres*, 116(D18), 2011~~

15 Dufлот, V., Bègue, N., Pouliquen, M. L., Goloub, P. and Metzger, J. M : Aerosols on the
16 Tropical Island of La Réunion (21° S, 55° E): Assessment of Climatology, Origin of Variability
17 and Trend. *Remote Sensing*, 14(19), 4945, 2022

18 ~~Eckhardt, S., Cassiani, M., Evangeliou, N., Sollum, E., Pisso, I., and Stohl, A.: Source-receptor~~
19 ~~matrix calculation for deposited mass with the Lagrangian particle dispersion model~~
20 ~~FLEXPART v10.2 in backward mode. *Geosci. Model Dev.*, 10, 4605–4618,~~
21 ~~<https://doi.org/10.5194/gmd-10-4605-2017>, 2017.~~

22 Edwards, D. P., Emmons, L. K., Gille, J. C., Chu, A., Attié, J. L., Giglio, L and Drummond, J.
23 R.: Satellite-observed pollution from Southern Hemisphere biomass burning. *Journal of*
24 *Geophysical Research: Atmospheres*, 111(D14), 2006

25 ~~Forster, C., Stohl, A., and Seibert, P.: Parameterization of convective transport in a Lagrangian~~
26 ~~particle dispersion model and its evaluation, *J. Appl. Meteorol. Clim.*, 46, 403–422, 2007.~~

27 ▲

28 Fromm, M., Lindsey, D. T., Servranckx, R., Yue, G., Trickl, T., Sica, R.: The untold story of
29 pyro-cumulonimbus. *Bulletin of the American Meteorological Society*, 91(9), 2010

30 Hamill, P., Jensen, E. J., Russell, P. B., and Bauman, J. J.: The life cycle of stratospheric aerosol
31 particles, *B. Am. Meteorol. Soc.*, 78, 1395–1410, [https://doi.org/10.1175/1520-](https://doi.org/10.1175/1520-0477(1997)078E2.0.CO;2)
32 [0477\(1997\)078E2.0.CO;2](https://doi.org/10.1175/1520-0477(1997)078E2.0.CO;2), 1997

Mis en forme : Police :Non Gras, Couleur de police :
Automatique

1 [Garstang, M., Tyson, P. D., Browell, E. and Swap, R. J.: . Large scale transport of biogenic](#)
2 [and biomass burning products. JS Levine, 389-395, 1996](#)

3 [Grythe, H., Kristiansen, N. I., Groot Zwaafink, C. D., Eckhardt, S., Ström, J., Tunved, P.,](#)
4 [Krejci, R., and Stohl, A.: A new aerosol wet removal scheme for the Lagrangian particle model](#)
5 [FLEXPART v10, Geosci. Model Dev., 10, 1447–1466. \[https://doi.org/10.5194/gmd-10-1447-\]\(https://doi.org/10.5194/gmd-10-1447-2017\)](#)
6 [2017, 2017.](#)

7 ▲
8 Haarig, M.; Ansmann, A.; Baars, H.; Jimenez, C.; Veselovskii, I.; Engelmann, R.; Althausen,
9 D. Depolarization and lidar ratios at 355, 532, and 1064 nm and microphysical properties of
10 aged tropospheric and stratospheric Canadian wildfire smoke. Atmos. Chem. Phys. 2018, 18,
11 11847–11861.

12 Hashimoto, M., Nakajima, T., Dubovik, O., Campanelli, M., Che, H., Khatri, P., Takamura, T
13 and Pandithurai, G: Development of a new data-processing method for SKYNET sky
14 radiometer observations. Atmospheric Measurement Techniques, 5(11), 2723-2737, 2012

15 Hauchecorne, A., Godin, S., Marchand, M., Heese, B., and Souprayen, C.: Quantification of
16 the transport of chemical constituents from the polar vortex to midlatitudes in the lower
17 stratosphere using the high-resolution advection model MIMOSA and effective diffusivity, J.
18 Geophys. Res.-Atmos., 107, 1–13, 2002

19 Héron, D., Evan, S., Brioude, J., Rosenlof, K., Posny, F., Metzger, J. M., & Cammas, J. P.:
20 Impact of convection on the upper-tropospheric composition (water vapor and ozone) over a
21 subtropical site (Réunion island; 21.1° S, 55.5° E) in the Indian Ocean. Atmospheric Chemistry
22 and Physics, 20(14), 8611-8626., 2020

23 Heese, B., Godin, S., and Hauchecorne, A.: Airborne lidar measurements of ozone filaments
24 during METRO—A validation of PV advection model MIMOSA, J. Geophys. Res, 106, 20011–
25 20024, 2001.

26 Holanda, B. A., Pöhlker, M. L., Walter, D., Saturno, J., Sörgel, M., Ditas, J and Pöhlker, C:
27 Influx of African biomass burning aerosol during the Amazonian dry season through layered
28 transatlantic transport of black carbon-rich smoke. Atmospheric Chemistry and Physics, 20(8),
29 4757-4785, 2020

30 Hu, Q., Goloub, P., Veselovskii, I., Bravo-Aranda, J.-A., Popovici, I. E., Podvin, T., Haeffelin,
31 M., Lopatin, A., Dubovik, O., Pietras, C., Huang, X., Torres, B., and Chen, C.: Long-range-

Mis en forme : Police :Non Gras, Couleur de police :
Automatique

Mis en forme : Police :Non Gras, Couleur de police :
Automatique

1 transported Canadian smoke plumes in the lower stratosphere over northern France, *Atmos.*
2 *Chem. Phys.*, 19, 1173–1193, <https://doi.org/10.5194/acp-19-1173-2019>, 2019.

3 Hurtmans, D., Coheur, P.F.; Wespes, C., Clarisse, L., Scharf, O., Clerbaux, C., Hadji-Lazaro,
4 J., George, M., Turquety, S: FORLI radiative transfer and retrieval code for IASI. *J. Quant.*
5 *Spectrosc. Radiat. Transf.* 2012, 113, 1391–1408, 2012

6 Jäger, H. and Deshler, T.: Lidar backscatter to extinction, mass and area conversions for
7 stratospheric aerosols based on midlatitude balloon borne size distribution measurements,
8 *Geophys. Res. Lett.*, 29, 1929, <https://doi.org/10.1029/2002GL015609>, 2002

9 Jones, N. B., Rinsland, C. P., Liley, J. B., and Rosen, J.: Correlation of aerosol and carbon
10 monoxide at 45 S: Evidence of BB emissions. *Geophysical research letters*, 28(4), 709-712.,
11 2001

12 Kablick III, G. P., Allen, D. R., Fromm, M. D. and Nedoluha, G. E: Australian pyroCb smoke
13 generates synoptic-scale stratospheric anticyclones, *Geophys. Res. Lett.*, 47(13),
14 e2020GL088101, 2020.

15 Khaykin, S., Legras, B., Bucci, S., Sellitto, P., Isaksen, L., Tence, F. and Godin-Beekmann, S:
16 The 2019/20 Australian wildfires generated a persistent smoke-charged vortex rising up to 35
17 km altitude. *Communications Earth & Environment*, 1(1), 1-12, 2020.

18 Khaykin, S. M., Godin-Beekmann, S., Hauchecorne, A., Pelon, J., Ravetta, F., and Keckhut, P:
19 Stratospheric smoke with unprecedentedly high backscatter observed by lidars above southern
20 France, *Geophys. Res. Lett.*, 1944, 8007, doi:10.1002/2017GL076763, 2018.

21 Kaufman, Y. J., Ichoku, C., Giglio, L., Korontzi, S., Chu, D. A., Hao, W. M and Justice, C. O.:
22 Fire and smoke observed from the Earth Observing System MODIS instrument--products,
23 validation, and operational use. *International Journal of Remote Sensing*, 24(8), 1765-1781,
24 2003

25 Klett, J. D.: Lidar inversion with variable backscatter/extinction ratios, *Appl. Opt.*, AO, 24,
26 1638–1643, <https://doi.org/10.1364/AO.24.001638>, 1985.

27 Kloss, C.; Sellitto, P., Von Hobe, M.; Berthet, G.; Smale, D.; Krysztofiak, G.; Legras, B.
28 Australian fires 2019–2020: Tropospheric and stratospheric pollution throughout the whole fire
29 season. *Front. Environ. Sci.* 2021, 9, 220, 2021

30 Kloss, C., Berthet, G., Sellitto, P., Ploeger, F., Bucci, S., Khaykin, S., Jégou, F., Taha, G.,
31 Thomason, L. W., Barret, B., Le Flochmoen, E., von Hobe, M., Bossolasco, A., Bègue, N., and
32 Legras, B.: Transport of the 2017 Canadian wildfire plume to the tropics via the Asian monsoon

1 circulation, Atmos. Chem. Phys., 19, 13547–13567, [https://doi.org/10.5194/acp-19-13547-](https://doi.org/10.5194/acp-19-13547-2019)
2 2019, 2019.

3 [Kloss, C., Sellitto, P., Renard, J. B., Baron, A., Bègue, N., Legras, B., Berthet, G., Briaud, E.,
4 Carboni, E., Duchamp, C., Duflot, V., Jacquet, P., Marquestaut, N., Metzger, J. M., Payen,
5 G., Ranaivombola, M., Roberts, T., Siddans, R. and Jegou, F.: Aerosol characterization of the
6 stratospheric plume from the volcanic eruption at Hunga Tonga 15 January 2022. *Geophysical
7 Research Letters*, 49\(16\), e2022GL099394., 2022](#)

8 Kremser, S., Thomason, L. W., Hobe, M., et al.: Stratospheric aerosol – Observations,
9 processes, and impact on climate, *Rev. Geophys.*, 54, 278–335, 2016.

10 [Labonne, M., Bréon, F. M and Chevallier, F.: Injection height of BB aerosols as seen from
11 a Labonne, M., Bréon, F. M., & Chevallier, F.; Injection height of biomass burning aerosols
12 as seen from a spaceborne lidar. *Geophysical research letters*, 34\(11\), 2007](#)

13 [Lashkari, H., Mohammadi, Z., and Keikhosravi, G.: Annual fluctuations and displacements
14 of inter tropical convergence zone \(ITCZ\) within the range of Atlantic Ocean-India. *Open
15 Journal of Ecology*, 7\(1\), 12-33, 2017, \[spaceborne lidar. *Geophysical Research Letters*, 34\\(11\\),
16 2017\]\(#\)](#)

17 Levin, N., Yebra, M. and Phinn, S.: Unveiling the factors responsible for Australia’s Black
18 Summer fires of 2019/2020. *Fire*, 4(3), 58, 2021

19 Livesey, N. J., Read, W. G., Wagner, P. A., Froidevaux, L., Santee, M. L., Schwartz, M. J.,
20 Lambert, A., Valle, L. F. M., Pumphrey, H. C., Manney, G. L., Fuller, R. A., Jarnot, R. F.,
21 Knosp, B. W., and Lay, R. R.: Version 5.0x Level 2 and 3 data quality and description
22 document., https://mls.jpl.nasa.gov/data/v5-0_data_quality_document.pdf, 2022.

23 de Mazière, M. D., Thompson, A. M., Kurylo, M. J., Wild, J. D., Bernhard, G., Blumenstock,
24 T. and Strahan, S. E: The Network for the Detection of Atmospheric Composition Change
25 (NDACC): history, status and perspectives, *Atmos. Chem. Phys.*, 18(7), 4935-4964, 2018

26 Morgan, W. T., Allan, J. D., Bauguitte, S., Darbyshire, E., Flynn, M. J., Lee, J and Coe, H:
27 Transformation and aging of biomass burning carbonaceous aerosol over tropical South
28 America from aircraft in-situ measurements during SAMBBA, 2019

29 Müller, D., Ansmann, A., Mattis, I., Tesche, M., Wandinger, U., Althausen, D., and Pisani, G.:
30 Aerosol-type-dependent lidar ratios observed with Raman lidar, *J. Geophys. Res.*, 112, D16202,
31 <https://doi.org/10.1029/2006JD008292>, 2007

Mis en forme : Police : (Par défaut) Times New Roman, 12 pt, Anglais (États-Unis)

Mis en forme : Anglais (États-Unis)

Mis en forme : Police : (Par défaut) Times New Roman, 12 pt, Anglais (États-Unis)

Mis en forme : Anglais (États-Unis)

Mis en forme : Police : Non Gras, Couleur de police : Automatique

Mis en forme : Police : Non Gras, Couleur de police : Automatique

1 Nakajima, T., Tonna, G., Rao, R., Kaufman, Y., and Holben, B.: Use of sky brightness
2 measurements from ground for remote sensing of particulate polydispersions. *Appl. Optics*, 35,
3 2672–2686, 1996

4 Neumann, C.: *Global guide to tropical cyclone forecasting*, WMO Trop. Cyclone Program Rep.
5 TCP-31, chap. Global Overview, World Meteorol. Organ., Geneva, Switzerland, 43 pp., 1993

6 Nicolae, D., Nemuc, A., Müller, D., Talianu, C., Vasilescu, J., Belegante, L. and Kolgotin, A.
7 : Characterization of fresh and aged BB events using multiwavelength Raman lidar and mass
8 spectrometry. *Journal of Geophysical Research: Atmospheres*, 118(7), 2956-2965, 2013

9 Ohneiser, K., Ansmann, A., Kaifler, B., Chudnovsky, A., Barja, B., Knopf, D. A and
10 Zamorano, F.: Australian wildfire smoke in the stratosphere: the decay phase in 2020/2021 and
11 impact on ozone depletion. *Atmospheric Chemistry and Physics*, 22(11), 7417, 2022

12 Ohneiser, K., Ansmann, A., Baars, H., Seifert, P., Barja, B., Jimenez, C and Wandinger, U.:
13 Smoke of extreme Australian bushfires observed in the stratosphere over Punta Arenas, Chile,
14 in January 2020: optical thickness, lidar ratios, and depolarization ratios at 355 and 532 nm.
15 *Atmospheric Chemistry and Physics*, 20(13), 8003-8015, 2020

16 Pisso, I., Sollum, E., Grythe, H., Kristiansen, N. I., Cassiani, M., Eckhardt, S., Arnold, D.,
17 Morton, D., Thompson, R. L., Groot Zwaafink, C. D., Evangeliou, N., Sodemann, H.,
18 Haimberger, L., Henne, S., Brunner, D., Burkhardt, J. F., Fouilloux, A., Brioude, J., Philipp, A.,
19 Seibert, P., and Stohl, A.: The Lagrangian particle dispersion model FLEXPART version 10.4,
20 *Geosci. Model Dev.*, 12, 4955–4997, <https://doi.org/10.5194/gmd-12-4955-2019>, 2019.

21

22 Portafaix, T., Morel, B., Bencherif, H., Baldy, S., Godin-Beekmann, S., and Hauchecorne, A.:
23 Fine-scale study of a thick stratospheric ozone lamina at the edge of the southern subtropical
24 barrier, *J. Geophys. Res.-Atmos.*, 108, D64196, <https://doi.org/10.1029/2002JD002741>, 2003.

25 Pumphrey, H. C., Filipiak, M. J., Livesey, J., Schwartz, M. J., Boone, C., Walker, K. A., Bernath,
26 P., Ricaud, P., Barret, B., Clerbaux, C., Jarnot, R. F., Manney, G. L. and Waters, J. W:
27 Validation of middle-atmosphere carbon monoxide retrievals from the Microwave Limb
28 Sounder on Aura, *J. Geophys. Res.*, 112, D24S38, doi: 10.1029/2007JD008723, 2007.

29 Russell-Smith, J.; Yates, C.P.; Whitehead, P.J.; Smith, R.; Craig, R.; Allan, G.E.; Thackway,
30 R.; Frakes, I.; Cridland, S.; Meyer, M.C.P.; et al. Bushfires' down under': Patterns and
31 implications of contemporary Australian landscape burning. *Int. J. Wildland Fire*, 16, 361–377,
32 2007

1 Sakai, T., T. Nagai, M. Nakazato, Y. Mano, and T. Matsumura: Ice clouds and Asian dust
2 studied with lidar measurements of particle extinction-to-backscatter ratio, particle
3 depolarization, and water vapor mixing ration over Tsukuba. *Applied Optics* 42 7103 –7116,
4 2003

5 Sakai, T., O. Uchino, T. Nagai, B. Liley, I. Morino, and T. Fujimoto: Long-term variation of
6 stratospheric aerosols observed with lidars over Tsukuba, Japan, from 1982 and Lauder, New
7 Zealand, from 1992 to 2015, *J. Geophys. Res. Atmos.*, 121, 10,283–10,293,
8 doi:10.1002/2016JD025132, 2016

9 Santee, M. L., Lambert, A., Manney, G. L., Livesey, N. J., Froidevaux, L., Neu, J. L. and Ward,
10 B. M: Prolonged and pervasive perturbations in the composition of the Southern Hemisphere
11 midlatitude lower stratosphere from the Australian New Year's fires. *Geophysical Research*
12 *Letters*, 49(4), e2021GL096270, 2022

13 Schwartz, M. J., Santee, M. L., Pumphrey, H. C., Manney, G. L., Lambert, A., Livesey, N. J.,
14 and Werner, F: Australian new year's pyrocb impact on stratospheric composition. *Geophysical*
15 *Research Letters*, 47(24), e2020GL090831, 2020

16 Schoeberl, M. R., Douglass, A. R., Hilsenrath, E., Bhartia, P. K., Barnett, J., Beer, R., Waters,
17 J., Gunson, M., Froidevaux, L., Gille, J., Levelt, P. F., and DeCola, P.: Overview of the EOS
18 Aura Mission, *IEEE Trans. Geosci. Remote Sens.*, 44, 1066–1074, 2006.

19 ~~Sellitto, P., Podglajen, A., Belhadji, R., Boichu, M., Carboni, E., Cuesta, J., C. Duchamp, C.~~
20 ~~Kloss, R. Siddans, N. Bègue, L. Blarel, F. Jegou, S. Khaykin, J. B. Renard. and Legras, B.:~~
21 ~~The unexpected radiative impact of the Hunga Tonga eruption of 15th January~~
22 ~~2022. *Communications Earth & Environment*, 3(1), 1–10., 2022~~

23 ~~Seibert, P. and Frank, A.: Source-receptor matrix calculation with a Lagrangian particle~~
24 ~~dispersion model in backward mode. *Atmos. Chem. Phys.*, 4, 51–63.~~
25 ~~<https://doi.org/10.5194/acp-4-51-2004>, 2004.~~

26 Sofiev, M., Ermakova, T. and Vankevich, R.: Evaluation of the smoke-injection height from
27 wild-land fires using remote-sensing data. *Atmospheric Chemistry and Physics*, 12(4), 1995–
28 2006, 2012

29 Solomon, S., Stone, K., Yu, P., Murphy, D. M., Kinnison, D., Ravishankara, A. R and Wang,
30 P: Chlorine activation and enhanced ozone depletion induced by wildfire aerosol,
31 *Nature*, 615(7951), 259-264, 2023

Mis en forme : Anglais (États-Unis)

1 [Stohl, A., Forster, C., Eckhardt, S., Spichtinger, N., Huntrieser, H., Heland, J., Schlager, H.,](#)
2 [Wilhelm, S., Arnold, F., and Cooper, O.: A backward modeling study of intercontinental](#)
3 [pollution transport using aircraft measurements, J. Geophys. Res., 108, 4370,](#)
4 [https://doi.org/10.1029/2002JD002862, 2003.](https://doi.org/10.1029/2002JD002862)

5
6 Swap, R. J., Annegarn, H. J., Suttles, J. T., King, M. D., Platnick, S., Privette, J. L and Scholes,
7 R. J: Africa burning: a thematic analysis of the Southern African Regional Science Initiative
8 (SAFARI 2000). Journal of Geophysical Research: Atmospheres, 108(D13), 2003

9 Taha, G., Loughman, R., Zhu, T., Thomason, L., Kar, J., Rieger, L. and Bourassa, A: OMPS
10 LP Version 2.0 multi-wavelength aerosol extinction coefficient retrieval algorithm.,
11 Atmospheric Measurement Techniques, 14(2), 1015-1036, 2021

12 Tencé, F., Jumelet, J., Bekki, S., Khaykin, S., Sarkissian, A. and Keckhut, P.: Australian Black
13 Summer smoke observed by lidar at the French Antarctic station Dumont d'Urville. Journal of
14 Geophysical Research: Atmospheres, 127(4), e2021JD035349, 2022

15 Turquet, S., Menut, L., Siour, G., Mailler, S., Hadji-Lazaro, J., George, M., Clerbaux, C.,
16 Hurtmans, D., Coheur, P.-F: APIFLAME v2.0 BB emissions model: Impact of refined input
17 parameters on atmospheric concentration in Portugal in summer 2016. Geosci. Model. Dev.,
18 2020, 13, 2981–3009, 2020.

19 Uchino, O., Tokunaga, M., Seki, K., Maeda, M., Naito, K., and Takahashi, K: Lidar
20 measurement of stratospheric transmission at a wavelength of 340 nm after the eruption of El
21 Chichon, J. Atmos. Terr. Phys., 45, 12, 849–850, 1983

22 Vernier, J. P., Pommereau, J. P., Garnier, A., Pelon, J., Larsen, N., Nielsen, J., and McDermid,
23 I. S., Tropical stratospheric aerosol layer from CALIPSO lidar observations, J. Geophys. Res.-
24 Atmos., 114, D00H10, <https://doi.org/10.1029/2009JD011946>, 2009

25 Wunch, D., Toon, G. C., Sherlock, V., Deutscher, N. M., Liu, C., Feist, D. G., and Wennberg,
26 P. O.: The Total Carbon Column Observing Network's GGG2014 Data Version, p. 43,
27 <https://doi.org/10.14291/tcon.ggg2014.documentation.R0/122>, 2015.

28 Young, S.A.: Analysis of lidar backscatter profiles in optically thin clouds, Appl. Opt., 34,
29 7019–7031., 1995

30 Xu, Y., Wang, W., Chen, B., Chang, M., & Wang, X.: Identification of ventilation corridors
31 using backward trajectory simulations in Beijing. Sustainable Cities and Society, 70, 102889,
32 2021

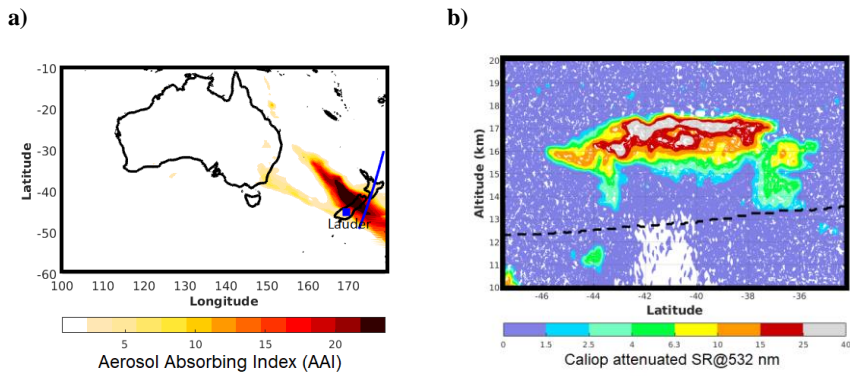
Mis en forme : Police :Non Gras, Couleur de police :
Automatique

1 Yu, P.; Davis, S.M.; Toon, O.B.; Portmann, R.W.; Bardeen, C.G.; Barnes, J.E.; Telg, H.;
2 Maloney, C.; Rosenlof, K.H. Persistent Stratospheric Warming due to 2019–2020 Australian
3 Wildfire Smoke. *Geophys. Res. Lett.* 2020, 2020, e2021GL092609, 2020
4 Yu, P., Davis, S. M., Toon, O. B., Portmann, R. W., Bardeen, C. G., Barnes, J. E and Rosenlof,
5 K. H: Persistent stratospheric warming due to 2019–2020 Australian wildfire
6 smoke. *Geophysical Research Letters*, 48(7), e2021GL092609, 2021
7 Zhou, M., Langerock, B., Vigouroux, C., Sha, M. K., Ramonet, M., Delmotte, M., ... & De
8 Mazière, M.: Atmospheric CO and CH₄ time series and seasonal variations on Reunion Island
9 from ground-based in situ and FTIR (NDACC and TCCON) measurements. *Atmospheric*
10 *Chemistry and Physics*, 18(19), 13881-13901, 2018

11

1
2
3
4
5

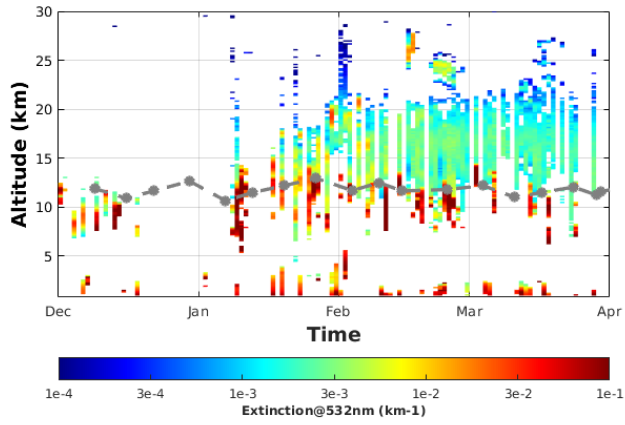
FIGURES AND TABLE



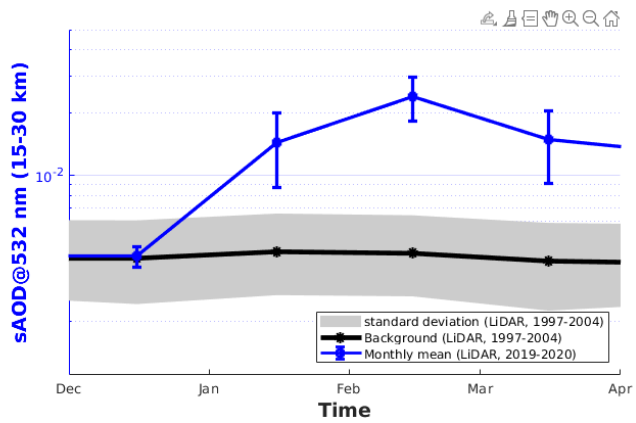
6 **Figure 1:** (a) Map of Aerosol Absorbing Index obtained from OMPS observations and (b)
7 scattering ratio profiles at 532 nm obtained from CALIOP observations on 1st January 2020.
8 The orbit overpass of CALIOP is indicated by the blue curve, while the blue square corresponds
9 to the Lauder site in plot (a). The black dashed line in (b) corresponds to the 380 K isentropic
10 level calculated from CALIOP observations.

11

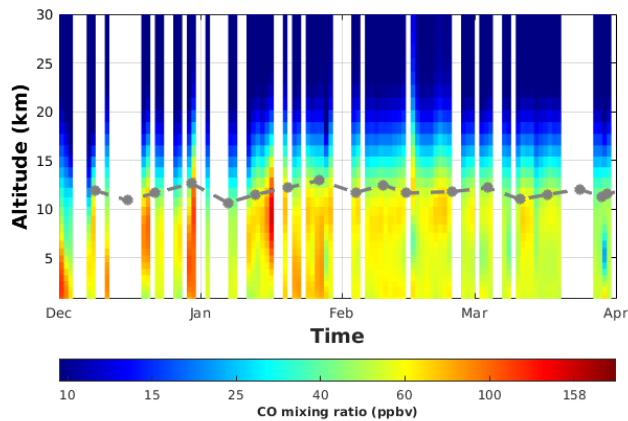
a)



b)



Mis en forme : Centré

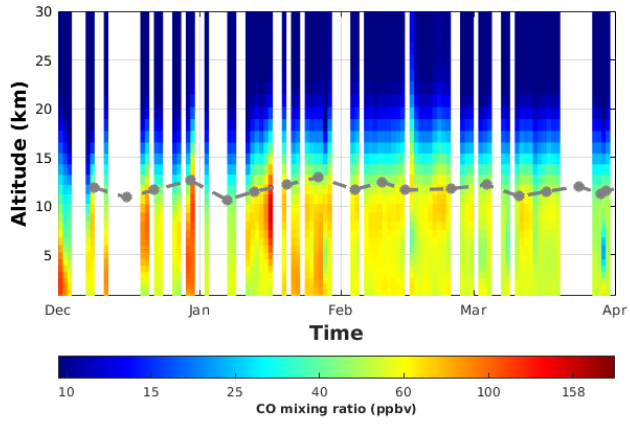


1 **Figure 2:** Time series of (a) daily profiles of aerosol extinction and (b) monthly mean of
 2 stratospheric AOD (sAOD between 15 and 30 km) at 532 nm obtained from lidar observations
 3 between 1st December 2019 and 1st April 2020. In order to screen non-aerosol contributors (such
 4 as clouds) to the extinction measurements, a mask based on the method reported by Nicolae et
 5 al. (2013), which includes consideration of plausible aerosols properties, was used. Specifically,
 6 we only kept profile parts with positive depolarization values, and Angström exponent ranges
 7 from 0.1 to 4. The grey line indicates the tropopause height obtained from radiosonde
 8 measurements. The background evolution of aerosol data and the associated standard deviation
 9 are given in black lines and grey areas, respectively. Time series of daily profiles at Lauder of
 10 (a) aerosol extinction at 532 nm obtained from lidar and (b) CO mixing ratio obtained from
 11 FTIR between 1st December 2019 and 1st April 2020. In order to screen non aerosol contributors
 12 (such as clouds) to the extinction measurements, a mask based on the method reported by
 13 Nicolae et al. (2013), which includes consideration of plausible aerosols properties, was used.
 14 Specifically, we only kept profile parts with positive depolarization values, and Angström
 15 exponent ranges from 0.1 to 4. The grey line indicates the tropopause height obtained from
 16 radiosonde measurements.

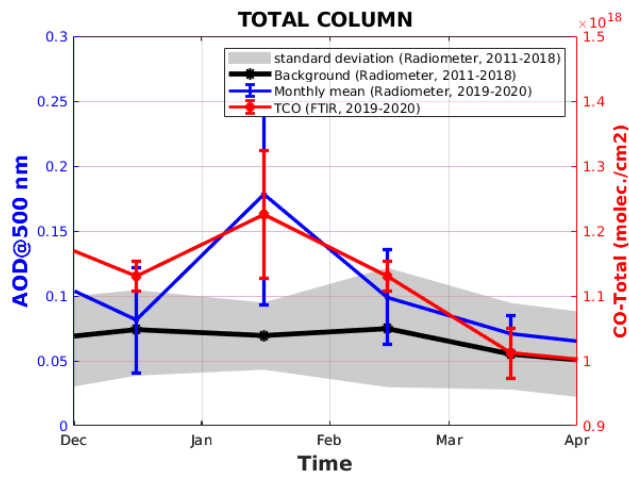
17

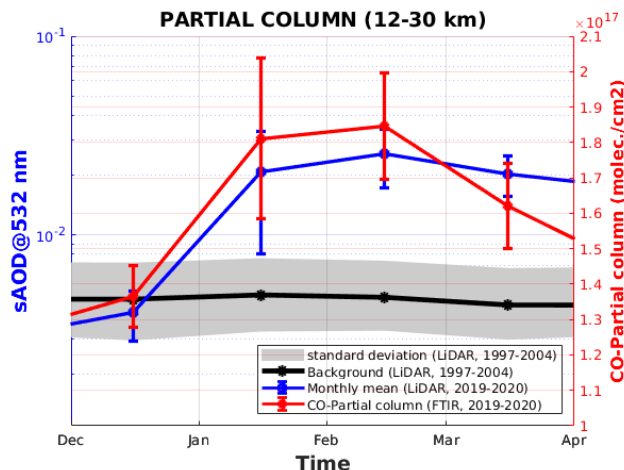
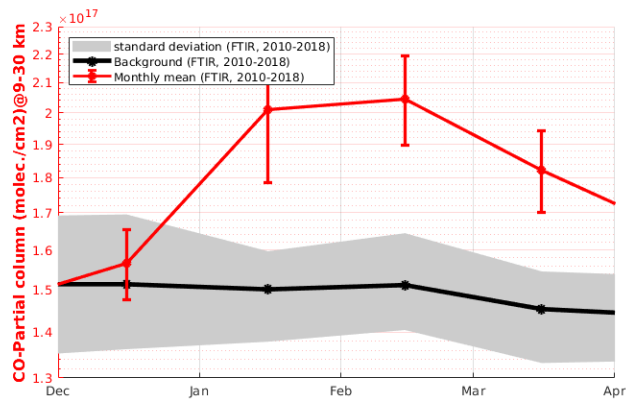
- Mis en forme : Police :Gras
- Mis en forme : Police :Gras
- Mis en forme : Couleur de police : Automatique
- Mis en forme : Police :Non Gras, Couleur de police : Automatique
- Mis en forme : Police :Non Gras, Couleur de police : Automatique
- Mis en forme : Police :Non Gras, Couleur de police : Automatique
- Mis en forme : Couleur de police : Automatique
- Mis en forme : Police :Non Gras, Couleur de police : Automatique
- Mis en forme : Couleur de police : Automatique
- Mis en forme : Police :Non Gras, Couleur de police : Automatique
- Mis en forme : Couleur de police : Automatique
- Mis en forme : Police :Non Gras, Couleur de police : Automatique
- Mis en forme : Couleur de police : Automatique
- Mis en forme : Police :Non Gras

a)



b)





1 **Figure 3:** Time series of (a) daily profiles of CO mixing ratio and (b) monthly mean of partial
 2 column of CO (between 9 and 30 km) obtained from FTIR at Lauder between 1st December
 3 2019 and 1st April 2020. The background evolution of the partial column of CO and the
 4 associated standard deviation are given in black lines and grey areas, respectively. (a) Monthly
 5 mean evolution of total column of aerosol (AOD at 500 nm) and CO obtained from the
 6 SKYNET radiometer and FTIR measurements respectively over Lauder from 1st December 2019 to 1st April
 7 2020. (b) Monthly mean evolution of the stratospheric AOD (sAOD) and CO (sCO) columns
 8 at Lauder between 1st December 2019 and 1st April 2020. The sAOD and sCO are calculated
 9 between 12 and 30 km from lidar and FTIR measurements respectively. The background
 10 evolution of aerosol data (AOD: 2011–2018 and sAOD: 1997–2004) and the associated standard
 11 deviation are given in black lines and grey areas, respectively.

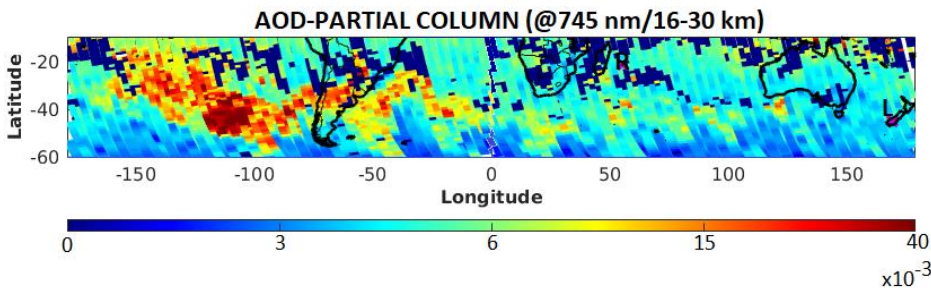
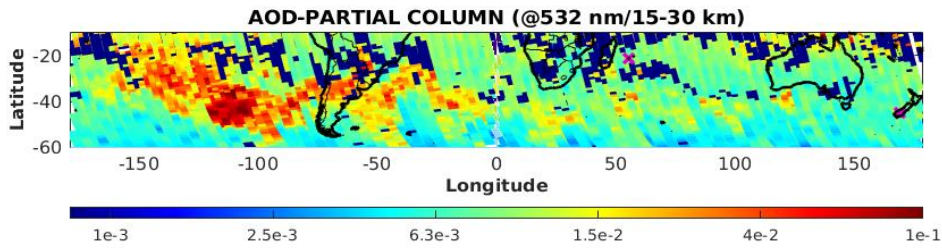
Mis en forme : Police :Non Gras, Couleur de police : Automatique

Mis en forme : Police :Non Gras

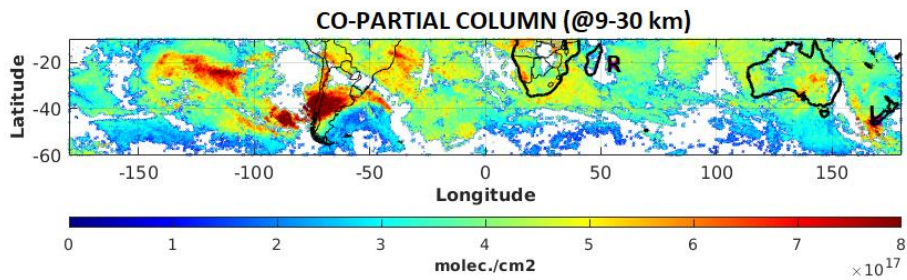
Mis en forme : Police :Non Gras, Couleur de police : Automatique

1
2

a)



b)



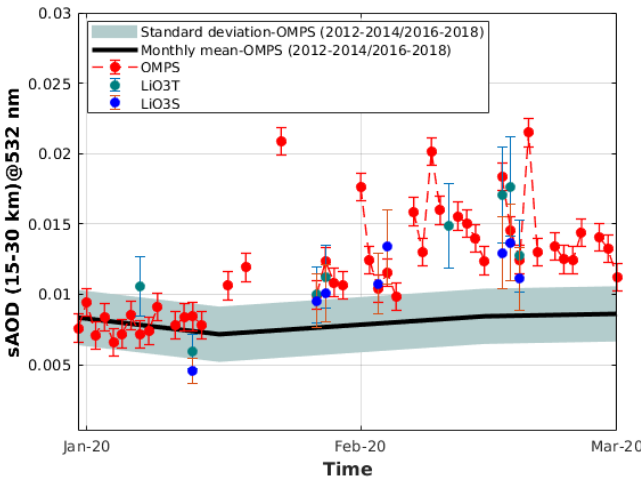
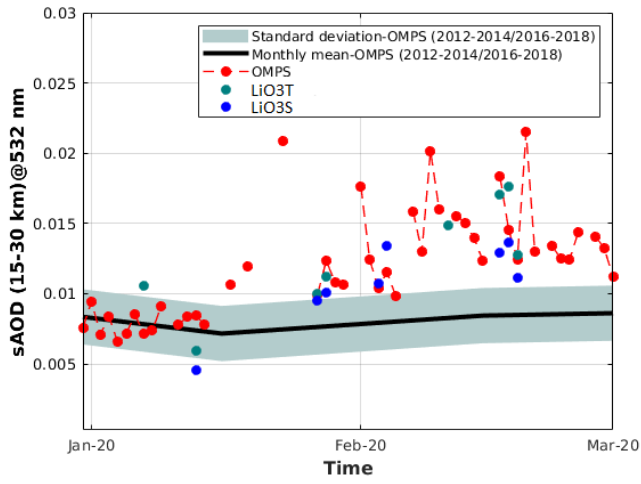
3 **Figure 4:** Time-averaged map (from 9th to 16th January 2020) of (a) sAOD (between 15 and 30
4 km at 532 nm) obtained from OMPS observations. Time-averaged map (from 9th to 16th January
5 2020) of (a) sAOD (between 16 and 30 km at 745 nm) obtained from OMPS observations and
6 (b) partial column of CO (averaged between 9 and 30 km) obtained from IASI observations.
7 The location of Reunion and Lauder sites are indicated by R and L respectively.

8

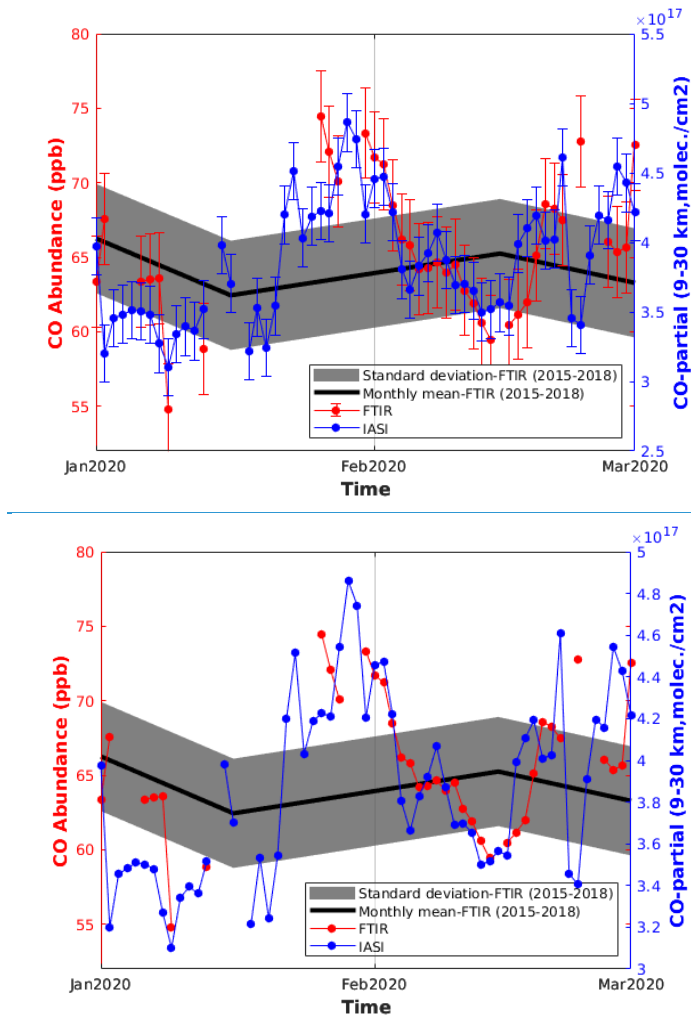
Mis en forme : Police : Non Gras, Couleur de police : Automatique

Mis en forme : Couleur de police : Automatique

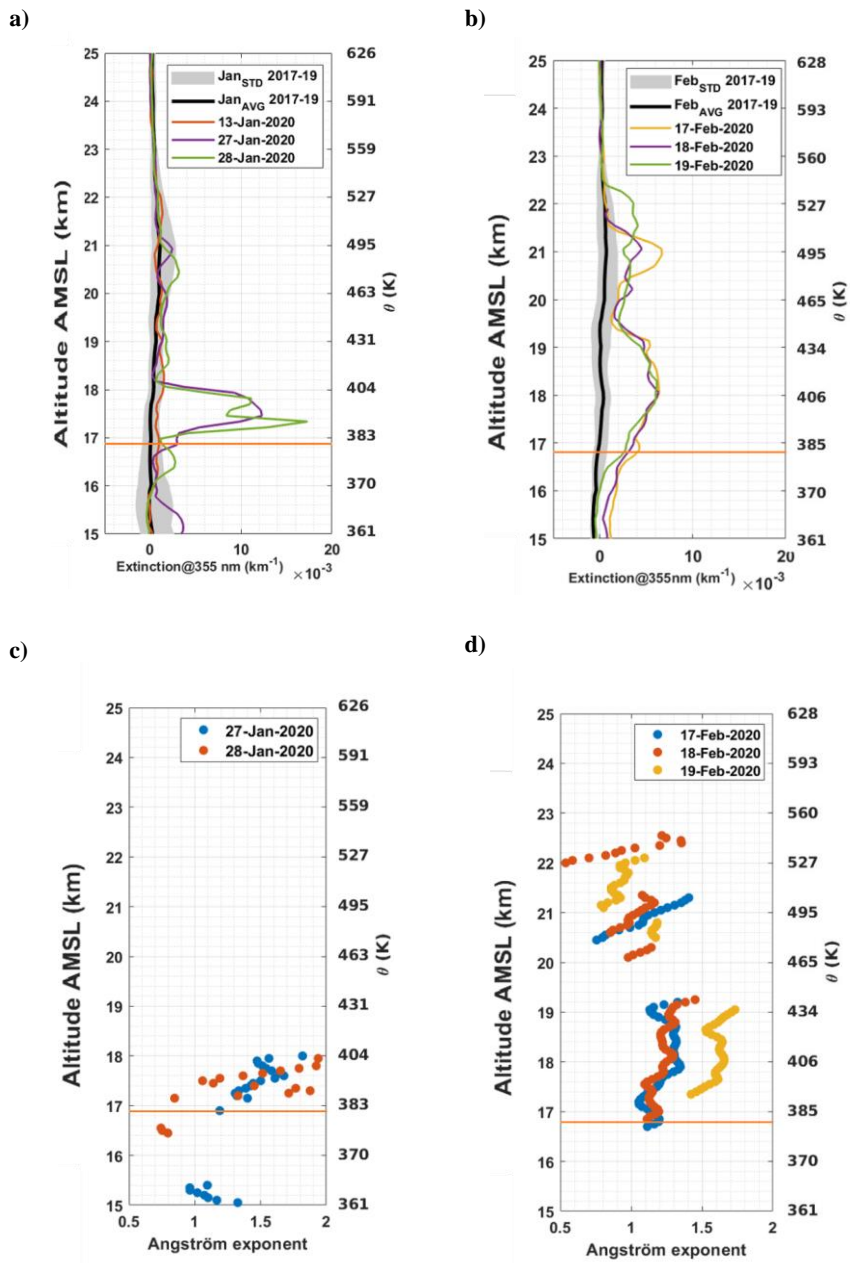
a)



b)

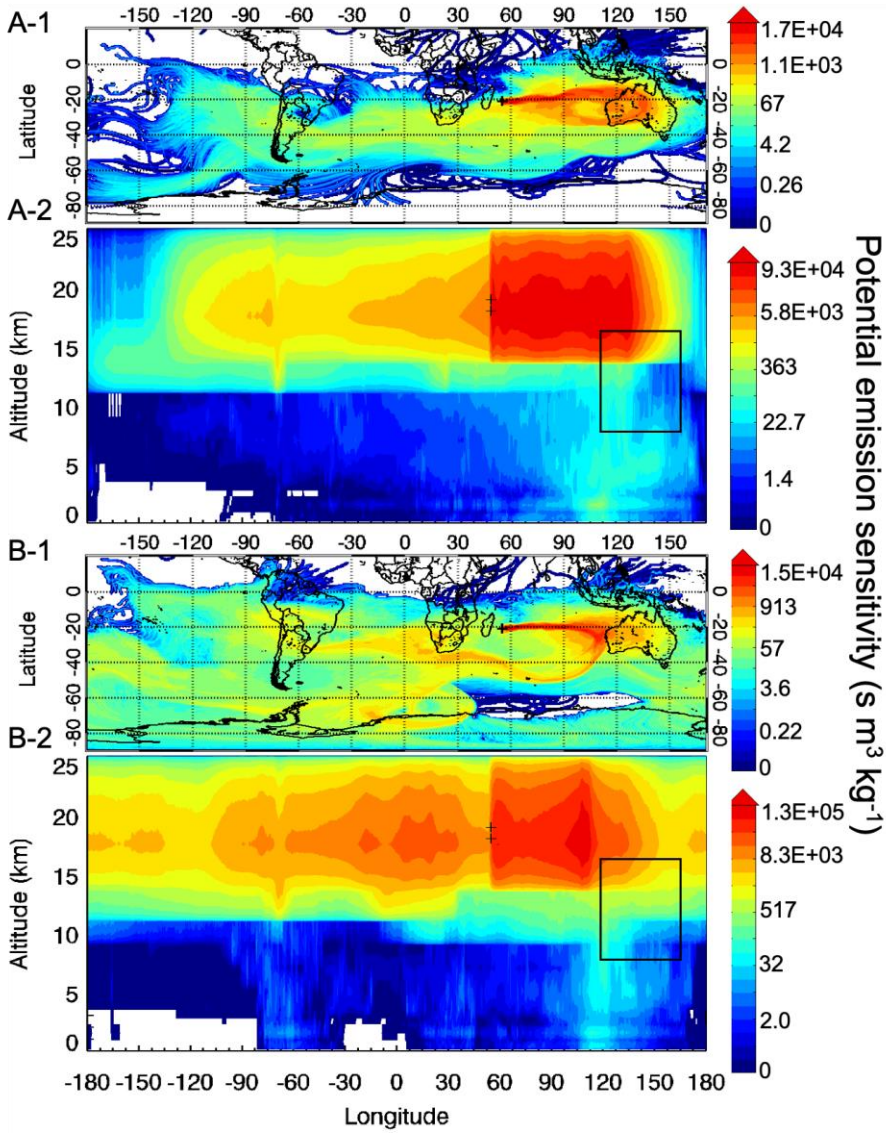


1 **Figure 5:** Daily mean evolution of aerosol (a) and CO (b) abundances obtained from ground-
 2 based and satellite observations at Reunion between 1st January and 1st March 2020. Partial
 3 column (molecule.cm⁻²) and abundance (ppb) of CO obtained from IASI (blue line) and FTIR
 4 (red line) respectively are given in the lower panel (b), while sAOD obtained from OMPS (red
 5 line) and Lidar (blue and green dots) are given in the upper panel (a). The black and dashed
 6 lines correspond to monthly mean and the associated standard deviation calculated during the
 7 background period.



1 **Figure 6:** Aerosol extinction (at 355 nm) (a, b) and Angström exponent (355-532 nm) (c, d)
 2 obtained from lidar observations at Reunion in the months January and February 2020. The
 3 tropopause height is indicated by the orange horizontal lines.

1

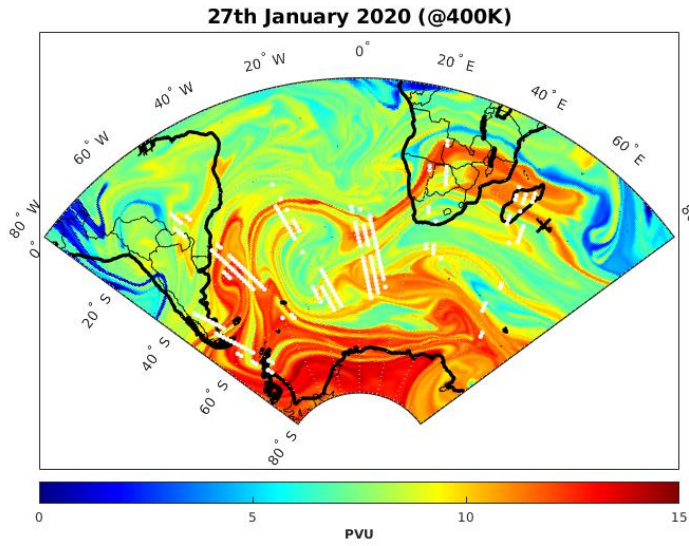


2

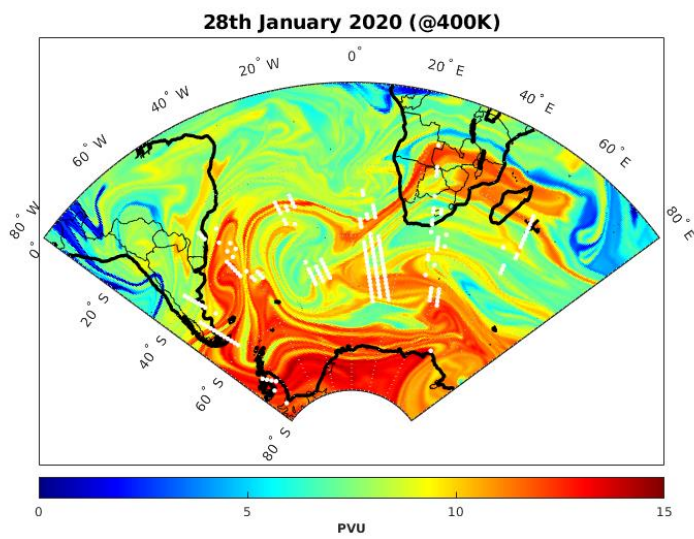
3 **Figure 7:** FLEXPART 30-day back trajectories initialized from Reunion (black cross) at 18 km
4 on 27th January 2020 (A-1-2) and 28th January 2020 (B-1-2). A-1 and B-1 correspond to an
5 integration of the trajectory positions over the whole altitude range. A-2 and B-2 are the vertical
6 view integrated over the whole latitude range of the back trajectories A-1 and B-1. The black
7 rectangle represented the injection height of the biomass burning aerosols.
8

1

a)



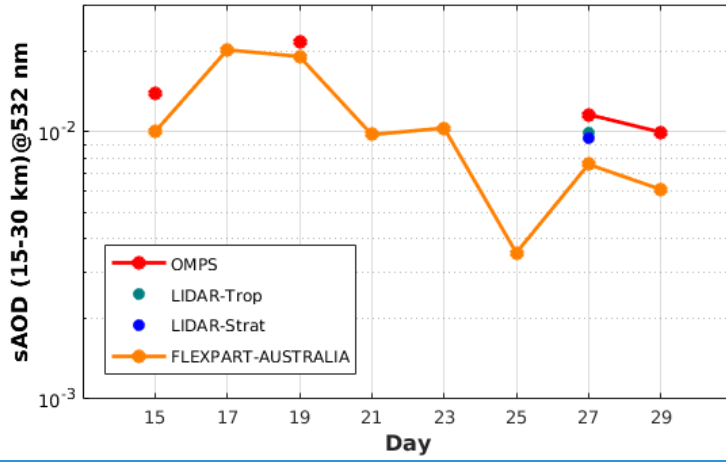
b)



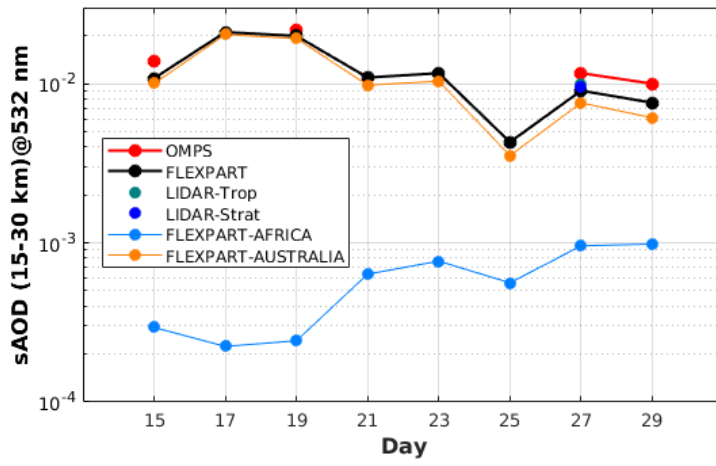
2 **Figure 8:** Advected PV map at the 400 K level obtained from the MIMOSA model (a) on 27
3 January 2022 and (b) on 28 January 2022. The white dots represent the localization of the
4 aerosol plume at $400\text{ K} \pm 5\text{ K}$ obtained from OMPS observations, while the black cross indicates
5 Reunion.
6

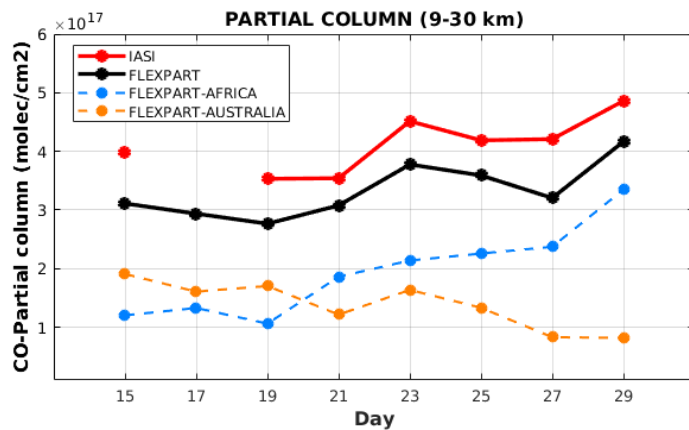
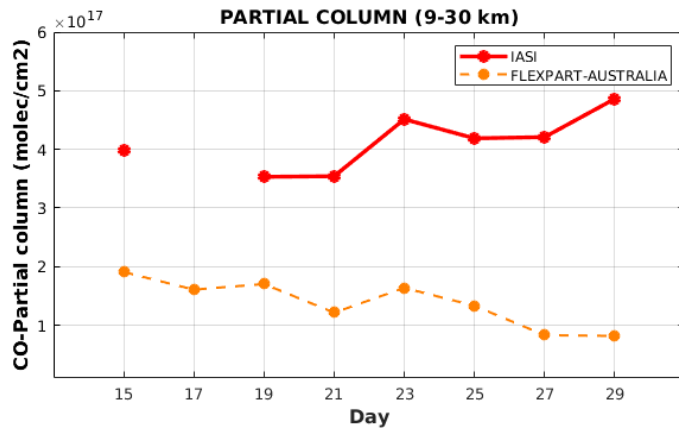
1

a)



b)



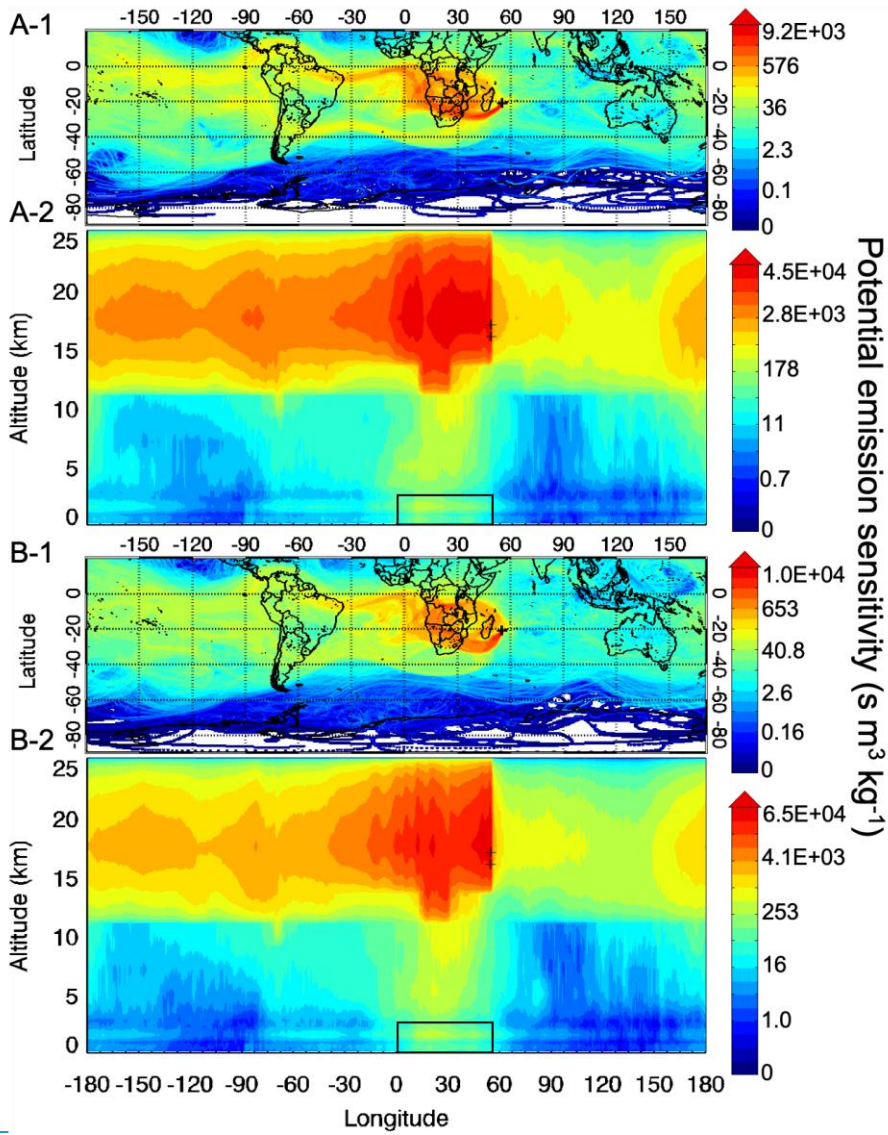


1 **Figure 9:** a) Daily evolution of sAOD (calculated between 15 and 30 km at 532 nm) obtained
 2 from OMPS-LP (red line), lidar (blue dots) and simulated by FLEXPART (orange black line)
 3 over Reunion from 15th to 29th January 2020. b) Daily evolution of partial column (calculated
 4 between 9 and 30 km) of CO observed by IASI (red line) and simulated by FLEXPART (orange
 5 black line) over Reunion from 15th to 29th January 2020. The CO evolution is simulated by
 6 FLEXPART considering only the CO emission (including BB and anthropogenic activity) from
 7 Australian emission. The simulated sAOD are calculated in considering only the aerosol
 8 emission (BC and OC) from Australian emission. The contribution from the African and
 9 Australian emission are in cyan line and orange line, respectively.

Mis en forme : Police :Non Gras, Couleur de police : Automatique

Mis en forme : Couleur de police : Automatique

1

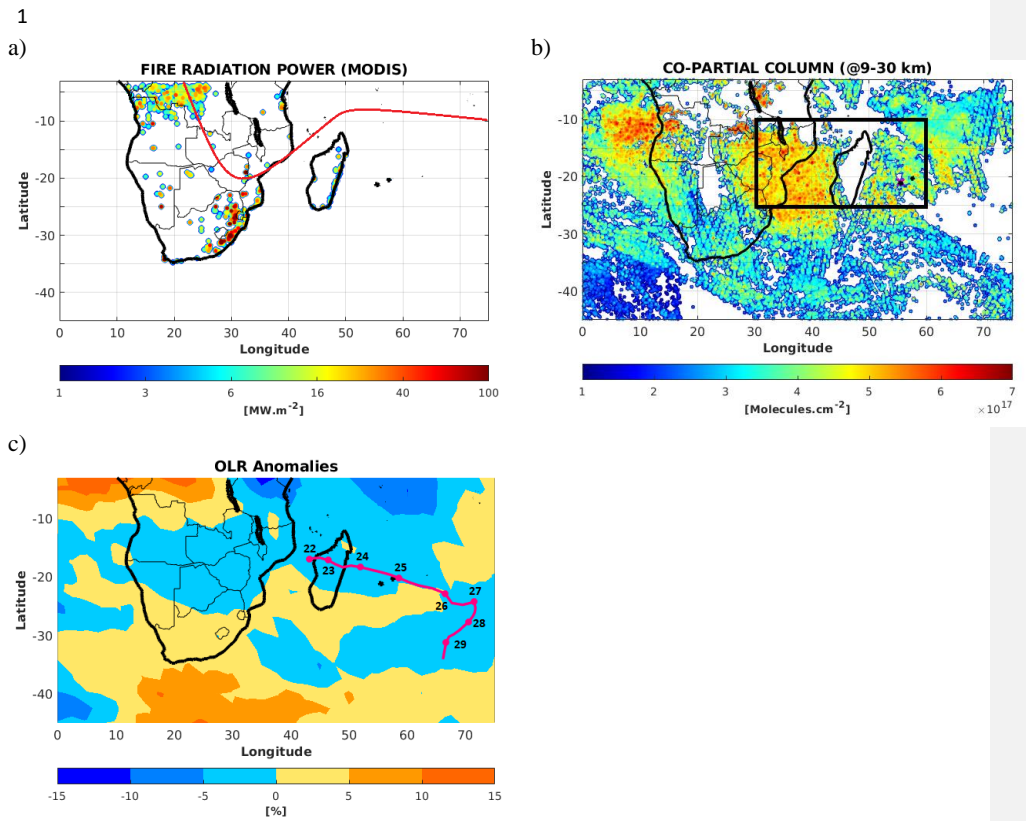


2

3

Figure 10: Same as figure 7 with an injection height initialized at 16 km.

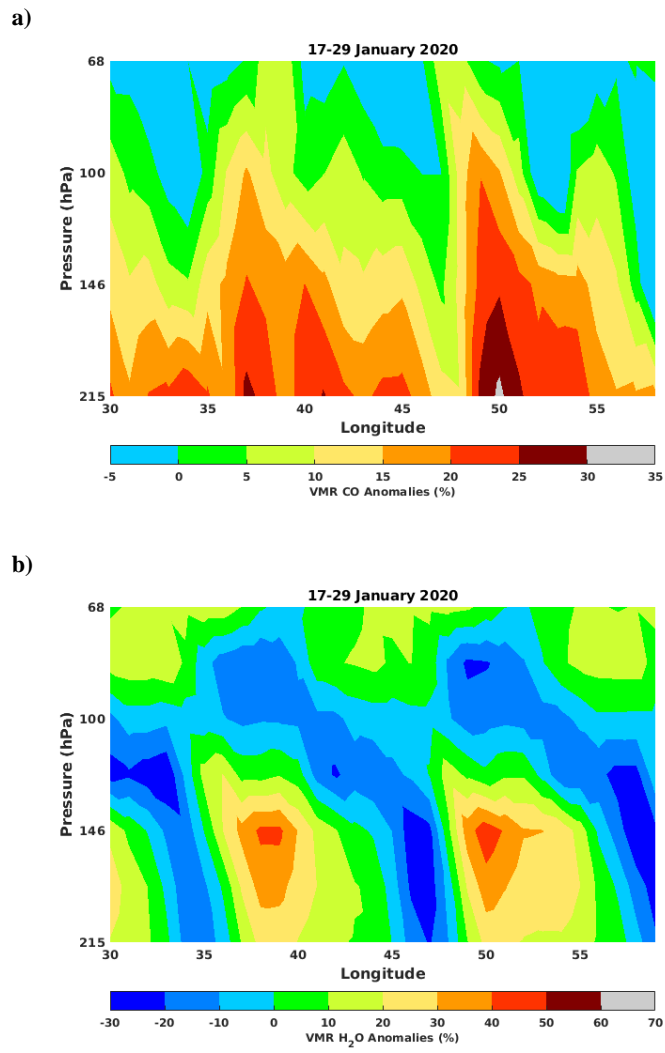
4



2 **Figure 10:** a) The total number of fire pixel and the associated fire radiative power obtained
 3 from MODIS observation between 16th and 29th January 2020. The red line indicates the
 4 average position of ITCZ (from Lashkari et al., 2017). b) Time-average map of partial column
 5 of CO (calculated between 9 and 30 km) obtained from IASI observations averaged between
 6 16th and 29th January 2020. The black square corresponds to the study domain where the vertical
 7 cross-section of CO and water vapor mixing ratio are calculated and reported in Figure 11. c)
 8 Time-average map of outgoing longwave radiation anomalies obtained from NCEP between
 9 16th and 29th January 2020. The red curve corresponds to the trajectory followed by the Diane
 10 strong tropical storm from 22nd to 29th January 2020. This trajectory is obtained from the RSMC
 11 (Regional Specialized Meteorological Center) of Reunion best-track database.
 12

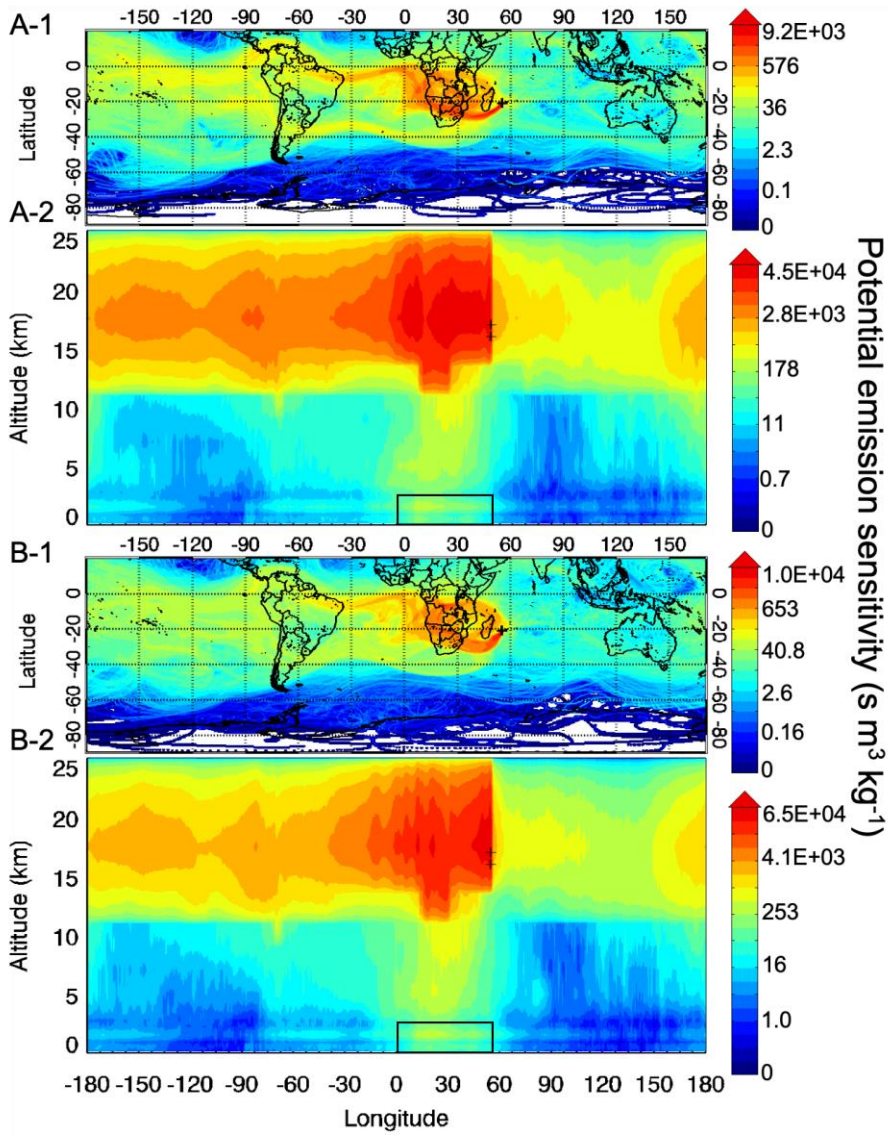
Mis en forme : Couleur de police : Automatique

1



2 **Figure 112:** Vertical cross section of (a) CO and (b) water vapor mixing ratio anomalies
3 obtained from MLS observation over southern Africa and the SWIO basin (black box in Figure
4 10b) between 16th and 29th January 2020.
5

1



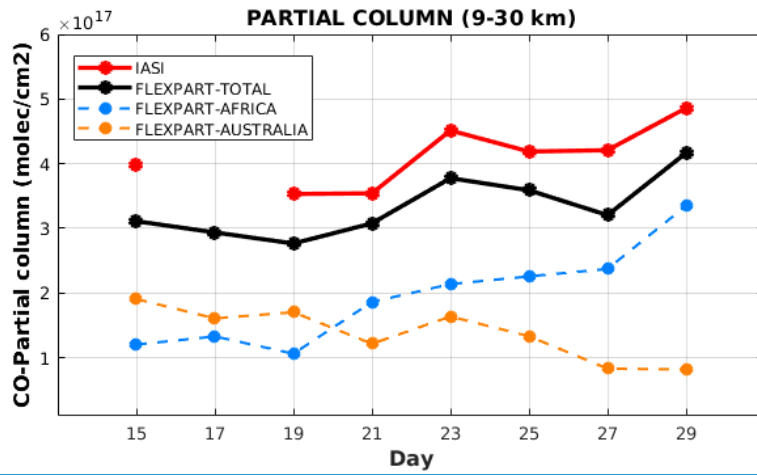
2

3

Figure 12: Same as figure 7 with an injection height initialized at 16 km.

4

1



2

[Figure 13: Daily evolution of partial column \(calculated between 9 and 30 km\) of CO observed by IASI \(red line\) and simulated by FLEXPART \(black line\) over Reunion from 15th to 29th January 2020. The CO evolution is simulated by FLEXPART considering only the CO emission \(including BB and anthropogenic activity\). The contribution from the African and Australian emission are in cyan line and orange line, respectively](#)

8